



Article

Spatial Downscaling of GRACE Data Based on XGBoost Model for Improved Understanding of Hydrological Droughts in the Indus Basin Irrigation System (IBIS)

Shoaib Ali ¹, Behnam Khorrami ², Muhammad Jehanzaib ³, Aqil Tariq ^{4,5,*}, Muhammad Ajmal ⁶, Arfan Arshad ⁷, Muhammad Shafeeque ⁸, Adil Dilawar ^{9,10}, Iqra Basit ¹¹, Liangliang Zhang ¹, Samira Sadri ¹², Muhammad Ahmad Niaz ¹³, Ahsan Jamil ¹⁴ and Shahid Nawaz Khan ¹⁵

¹ School of Water Conservancy & Civil Engineering, Northeast Agricultural University, Harbin 150030, China

² Department of GIS, The Graduate School of Applied and Natural Sciences, Dokuz Eylul University, 35220 Izmir, Turkey

³ Research Institute of Engineering and Technology, Hanyang University, Ansan 15588, Republic of Korea

⁴ Department of Wildlife, Fisheries and Aquaculture, College of Forest Resources, Mississippi State University, 775 Stone Boulevard, Starkville, MS 39762, USA

⁵ State Key Laboratory of Information Engineering in Surveying, Mapping and Remote Sensing, Wuhan University, Wuhan 430079, China

⁶ Department of Agricultural Engineering, University of Engineering & Technology, Peshawar 25120, Pakistan

⁷ Department of Biosystems and Agricultural Engineering, Oklahoma State University, Stillwater, OK 74078, USA

⁸ Institute of Geography, University of Bremen, 28359 Bremen, Germany

⁹ State Key Laboratory of Resource and Environmental Information System, Institute of Geographic Sciences and Natural Resources Research, Chinese Academy of Sciences, Beijing 100101, China

¹⁰ University of Chinese Academy of Sciences, Beijing 100049, China

¹¹ Remote Sensing, GIS, and Climate Research Lab (National Center of GIS and Space Application), Centre for Remote Sensing, University of The Punjab, Lahore 54590, Pakistan

¹² Department of Water Resources Engineering, Shahid Chamran University of Ahvaz, Ahvaz 6135783151, Iran

¹³ Department of Computer Science, Islamia University, Bahawalpur 63100, Pakistan

¹⁴ Department of Plant and Environmental Sciences, New Mexico State University, 3170S Espina Str., Las Cruces, NM 88003, USA

¹⁵ Geospatial Sciences Center of Excellence, Department of Geography and Geospatial Sciences, South Dakota State University, Brookings, SD 57007, USA

* Correspondence: at2139@msstate.edu or aqiltariq@whu.edu.cn



Citation: Ali, S.; Khorrami, B.; Jehanzaib, M.; Tariq, A.; Ajmal, M.; Arshad, A.; Shafeeque, M.; Dilawar, A.; Basit, I.; Zhang, L.; et al. Spatial Downscaling of GRACE Data Based on XGBoost Model for Improved Understanding of Hydrological Droughts in the Indus Basin Irrigation System (IBIS). *Remote Sens.* **2023**, *15*, 873. <https://doi.org/10.3390/rs15040873>

Academic Editors: Jolanta Nastula and Monika Birylo

Received: 12 December 2022

Revised: 29 January 2023

Accepted: 31 January 2023

Published: 4 February 2023



Copyright: © 2023 by the authors. Licensee MDPI, Basel, Switzerland. This article is an open access article distributed under the terms and conditions of the Creative Commons Attribution (CC BY) license (<https://creativecommons.org/licenses/by/4.0/>).

Abstract: Climate change may cause severe hydrological droughts, leading to water shortages which will require to be assessed using high-resolution data. Gravity Recovery and Climate Experiment (GRACE) satellite Terrestrial Water Storage (TWSA) estimates offer a promising solution to monitor hydrological drought, but its coarse resolution (1°) limits its applications to small regions of the Indus Basin Irrigation System (IBIS). Here we employed machine learning models such as Extreme Gradient Boosting (XGBoost) and Artificial Neural Network (ANN) to downscale GRACE TWSA from 1° to 0.25°. The findings revealed that the XGBoost model outperformed the ANN model with Nash Sutcliff Efficiency (NSE) (0.99), Pearson correlation (R) (0.99), Root Mean Square Error (RMSE) (5.22 mm), and Mean Absolute Error (MAE) (2.75 mm) between the predicted and GRACE-derived TWSA. Further, Water Storage Deficit Index (WSDI) and WSD (Water Storage Deficit) were used to determine the severity and episodes of droughts, respectively. The results of WSDI exhibited a strong agreement when compared with the Standardized Precipitation Evapotranspiration Index (SPEI) at different time scales (1-, 3-, and 6-months) and self-calibrated Palmer Drought Severity Index (sc-PDSI). Moreover, the IBIS had experienced increasing drought episodes, e.g., eight drought episodes were detected within the years 2010 and 2016 with WSDI of −1.20 and −1.28 and total WSD of −496.99 mm and −734.01 mm, respectively. The Partial Least Square Regression (PLSR) model between WSDI and climatic variables indicated that potential evaporation had the largest influence on drought after precipitation. The findings of this study will be helpful for drought-related decision-making in IBIS.

Keywords: Indus Basin Irrigation System; GRACE; TWS; machine learning models; downscaling; drought monitoring

1. Introduction

Being recognized as a highly destructive natural disaster, drought has significantly impacted society, the economy [1–4], and the agricultural sector [5]. The terrestrial water balance is being constantly disrupted as a direct and indirect result of the increasing human activities (e.g., water withdrawal, infrastructure development, deforestation, etc.) at global to regional scales [6,7]. The historical measurements and simulations of different hydrological fluxes, including soil moisture, precipitation, and discharge, demonstrate decreasing trends in many regions of the globe during the last several years [8–13]. Numerous regions of the globe are experiencing a rise in the frequency and severity of droughts [14,15] as a result of global warming [16,17] and Pacific variability [18]. Due to changes in precipitation and increased evaporation, it is anticipated that the drying trends will persist and intensify in the future climate [19]. Considering the wide-ranging impacts and complicated nature of drought, several worldwide studies and rising efforts have so far been directed toward drought detection, monitoring, planning, and mitigation [20].

Similar to other regions, most Pakistani regions are challenged with hydrometeorological extremes. Prolonged dry situations could be catastrophic and are unfavorable for cultivation, water and forest management, livestock, human safety, and food security [21]. Pakistan is one of the arid climate regions with limited precipitation and high temperatures [22,23]. Drought mainly occurs in the country due to rain shortages during the monsoon season [24]. The side effects of droughts are deeply sensed in Pakistan because its economy highly depends on agriculture [24,25]. Climate change has had serious ramifications for the socioeconomic and environmental conditions in Pakistan as well as its surrounding countries in Southwest Asia [26]. The Pacific Economic Survey report [27] expresses that drought incidents afflict the country's economy harshly, necessitating the careful and regular monitoring of drought in Pakistan.

Generally, drought is categorized into several classes, such as meteorological, agricultural, hydrological, groundwater, and socioeconomic drought [5,28–30]. Meteorological drought begins when there is a deficiency in precipitation across a region. Agricultural drought occurs due to a lack of soil moisture at a crucial moment during the growing season, while hydrological drought arises due to a decrease in streamflow and groundwater. During a groundwater drought incident, the groundwater level and discharge rates start to diminish due to decreased groundwater recharge rates in a drought-beaten aquifer [31]. Socioeconomic drought is the adverse impact of the aforementioned drought categories on different aspects of human life, such as increasing goods prices and population displacement [32,33]. The point-wise data of hydrological variables such as soil moisture, streamflow, groundwater levels, and surface water are needed to compute water deficits to measure hydrological droughts. Still, these observations are typically much more restricted in time and space than meteorological variables. Additionally, it is difficult to assess global variations of hydrological droughts since direct observations of surface hydrological indicators are often inconsistent and inconsecutive [34–36]. Evaluation of hydrological droughts is laborious because of the lack of high-quality hydrological records with appropriate temporal and geographic coverage [37].

Drought damages are significantly larger compared to other natural catastrophes, such as the 2012 drought in the United States, which caused \$12 billion in damage, most of which came from agricultural losses [38]. Droughts are expected to become more common in the coming decades, and human exposure to water scarcity is predicted to rise because of population growth and the climate crisis [39]. Identifying the spatio-temporal characteristics of droughts is essential for reducing the negative consequences of drought

risks, particularly in vulnerable areas [40]. Therefore, monitoring and characterizing drought events at the spatio-temporal scale of drought conditions is significant.

The Indus River is the primary water source for Pakistan. Pakistan has seen a rise in severe weather extremes and is highly vulnerable to climate change, such as droughts that afflicted 3.3 million people and resulted in a 2.6 percent decline in the Pakistani agriculture industry in 2002 [41]. A severe drought in India between 2002 and 2014 affected more than 300 million people, and in 2017 severe drought in Southern India affected more than 0.3 million people [42]. Zhou et al. [43] observed the response of vegetation to rainfall anomalies for drought evaluation over the Indus Basin from 2001 to 2018. Elbeltagi et al. [44] used hydrometeorological factors, GRACE satellite data, an improved Support Vector Machine (SVM), and a greedy regression technique to forecast the Combined Terrestrial Evapotranspiration Index (CTEI) in the Ganga River Basin. Drought occurrence and water deficit are related, especially in dry regions, such that a greater water deficit might increase the intensity of a drought and the other way around [43,45]. Exploring the prevalent characteristics of drought for distinct climatic regimes and impact domains aids in developing more precise identification systems capable of describing the progression of drought conditions in space and time [46].

Drought is a complex phenomenon trickling down to multiple sectors globally. It cannot be characterized easily due to the lack of a universally accepted definition and variability across the sectors [47]. However, drought indicators that include drought-related environmental factors can be used to characterize drought duration and severity [28]. The drought in Senegal was characterized using the GRACE-derived Terrestrial Water Storage Deficit Index (TWSI) during the studied period (April 2002–December 2021). The findings demonstrated good associations among the GRACE estimates, Standardized Temperature Index (STI), and Standardized Precipitation Index (SPI) in some years and seasons [48]. Alshehri et al. [49] observed the rising anthropogenic impact on GRACE-derived terrestrial water storage and groundwater storage variations in Wadi As-Sirhan, Northern Saudi Arabia, from 2002 to 2021. The groundwater was overexploited due to agricultural expansion over recent decades in Wadi As-Sirhan. Thailand's Chao Phraya River Basin (CPRB) is very susceptible to extreme events. The past droughts and floodings (e.g., 2004, 2007, 2011, 2015) in this basin have engendered tremendous costs for Thailand as well as the global economy by disrupting the industrial production of global supply chains of the neighboring countries [50]. Moreover, the basin was revealed to have a great potential for severe droughts, based on the recently developed Drought Potential Index (DPI) [50]. For the calculation of drought indicators, such as the SPI, Palmer Drought Severity Index (PDSI), and Standardized Runoff Index, ground-based point measurements are required (SRI) [47]. Traditional methods are not sufficient to detect the sophisticated spatial pattern of drought conditions at a regional scale in locations with few observations (e.g., Northeast China, Indus River Basin, and hilly regions) [51].

The general approach to investigating and categorizing droughts relies on the field-based observations of hydrometeorological variables received from stations and spatially mapped through interpolation techniques. However, the applicability of these traditional techniques is shackled by some challenges. Since the processed data are point-wise and sparsely distributed throughout the region, the spatial portrayal of the drought characteristics through interpolation techniques is challenging [52]. Furthermore, the single-variable-based construction of drought indices may not reflect the actual drought situation properly [46]. The Standardized Precipitation Evapotranspiration Index (SPEI) is an extended version of SPI generated by incorporating Potential Evapotranspiration (PET) in determining drought [53]. In addition, the Palmer Drought Severity Index (PDSI) [54], the self-calibrated Palmer Drought Severity Index (sc-PDSI) [55], and Multivariate Standardized Drought Index (MSDI) [56] are widely used drought indices. According to previous studies, climate change triggers more frequent and severe natural disasters [57,58]. It is projected that the severity, frequency, and length of several climate-induced events will rise

by the end of the century [59]. Therefore, drought assessment and prediction studies are of predominant importance.

Currently, remote sensing offers continuous and reliable measurements of surface moisture status, and these satellite-derived data have resulted in significant advancements in drought monitoring [5,60]. Previous works such as Qi et al. [61], Gu et al. [62], Long et al. [63], and Yi and Wen [64] utilized remote sensing-based products, including Moderate Resolution Imaging Spectroradiometer (MODIS) and GRACE for drought analysis. The multidecadal characteristics of droughts in Peninsular India were evaluated based on the surface water and groundwater water storage deficits [65]. According to Niemeier [66], remote sensing-based drought metrics have created a new pathway for detecting and monitoring droughts by making it possible to gather precise spatial data on a regional to global domain, with high dependability and a high repetition rate.

The spatial resolution of the GRACE level 2 datasets is $\sim 3 \times 3^\circ$ which are processed by three data processing centers, including the Center for Space Research (CSR), Jet Propulsion Laboratory (JPL), and GeoForschungsZentrum Potsdam (GFZ), to generate the level 3 gridded data. The level 3 data are in the forms of spherical harmonic solutions (SH) and mascon solutions (Mascons) with a spatial resolution of 1° for the SH and $0.5\text{--}0.25^\circ$ for the Mascons [67,68]. We applied the SH gridded data from the three data processors [69,70]. The SH datasets have less uncertainty than Mascon products when estimating water storage [71], justifying their widespread applications in the Indus Basin [71–76]. Besides, the spatially improved Level 3 products (with a resolution of 0.25° to 0.5°) contain less physical information than the original GRACE datasets [67,77]. The GRACE-SH data can be more suitable for the local-scale assessment and analysis through downscaling processes to create a higher spatial resolution (0.25°) [78,79].

Although the current resolution (~ 100 km) of the GRACE estimates paved the way for deriving helpful information regarding hydrological droughts, its coarse resolution impedes its feasibility for local/regional scale monitoring [52]. Therefore, hydrological measurements are necessary at a higher resolution to have a better and more precise estimation of droughts. To this end, machine learning algorithms were developed to solve this problem [80,81]. For instance, Chen et al. [82] used the Random Forest (RF) algorithm to downscale TWS and GWS parameters by integrating six hydrological variables. They achieved the highest NSE and R of 0.68 and 0.83, respectively. Yin et al. [83] suggested that the evapotranspiration (ET) data can be applied to downscale GWS in areas, such as the North China Plain, where a robust connection exists between GRACE-derived GWS and ET data. Rahaman et al. [84] reported an enhanced NSE (from 0.58 to 0.84) for the RF-based downscaled GWS in the Northern High Plains aquifer. Ali et al. [76] downscaled the GRACE data in the Irrigated Indus Basin Irrigation System, and R reached 0.67–0.97. However, the IBIS has not been used to investigate the characteristics of hydrological drought based on downscaled GRACE data. To investigate the drought conditions in the IBIS from 2003 to 2016, we employed the Water Storage Deficit Index (WSDI), primarily focusing on using the downscaled products.

Previous work from Ning et al. [85] to downscale the TWS and GWS, Rahaman et al. [84], Chen et al. [82], and Ali et al. [78] examined the downscaling of GRACE data in different regions around the world to study variations in water storage for small-scale regions. However, these studies do not consider the high-resolution data in a drought characterization framework for quantifying drought severity. Despite the widespread use of remote sensing-based products, various limitations, such as missing data owing to clouds, vegetation reactions, and coarse resolution, have limited their practical applicability. Improving the spatial resolution of remotely sensed products is of utmost importance for reliable and detailed drought analysis. Therefore, this study presents a novel approach to drought severity assessment which was lacking in previous studies. The main objective of this research includes (1) the development of a machine learning-based approach to enhance the coarse resolution of GRACE TWSA data from the current 1° to 0.25° , (2) the application of the downscaled TWSA database to estimate drought events and severity

using Water Storage Deficit (WSD) and Water Storage Deficit Index (WSDI) in the Indus Basin Irrigation System (IBIS), (3) spatio-temporal analysis of WSDI based on downscaled TWSA, and (4) analysis of the contribution of climatic indicators to WSDI based on Partial Least Square Regression (PLSR) model.

2. Materials and Methods

2.1. Study Area

The Indus Basin Irrigation System (IBIS) (Figure 1) stretches from the Northside of the Himalayas to the dry alluvial Plains in the south of Pakistan and covers approximately 201,072 km² of Pakistan territory. It was selected as a study area owing to harsh drought events that have transpired in the basin over the past years [5,11]. This region is vulnerable to more frequent and intense drought events due to climate change impacts, a phenomenon that significantly influences Pakistan's food, water security, and economic conditions [71,86,87]. Approximately 61% of the Indus Basin area exists in Pakistan and is a predominant source of irrigation, water supply, and hydropower [88].

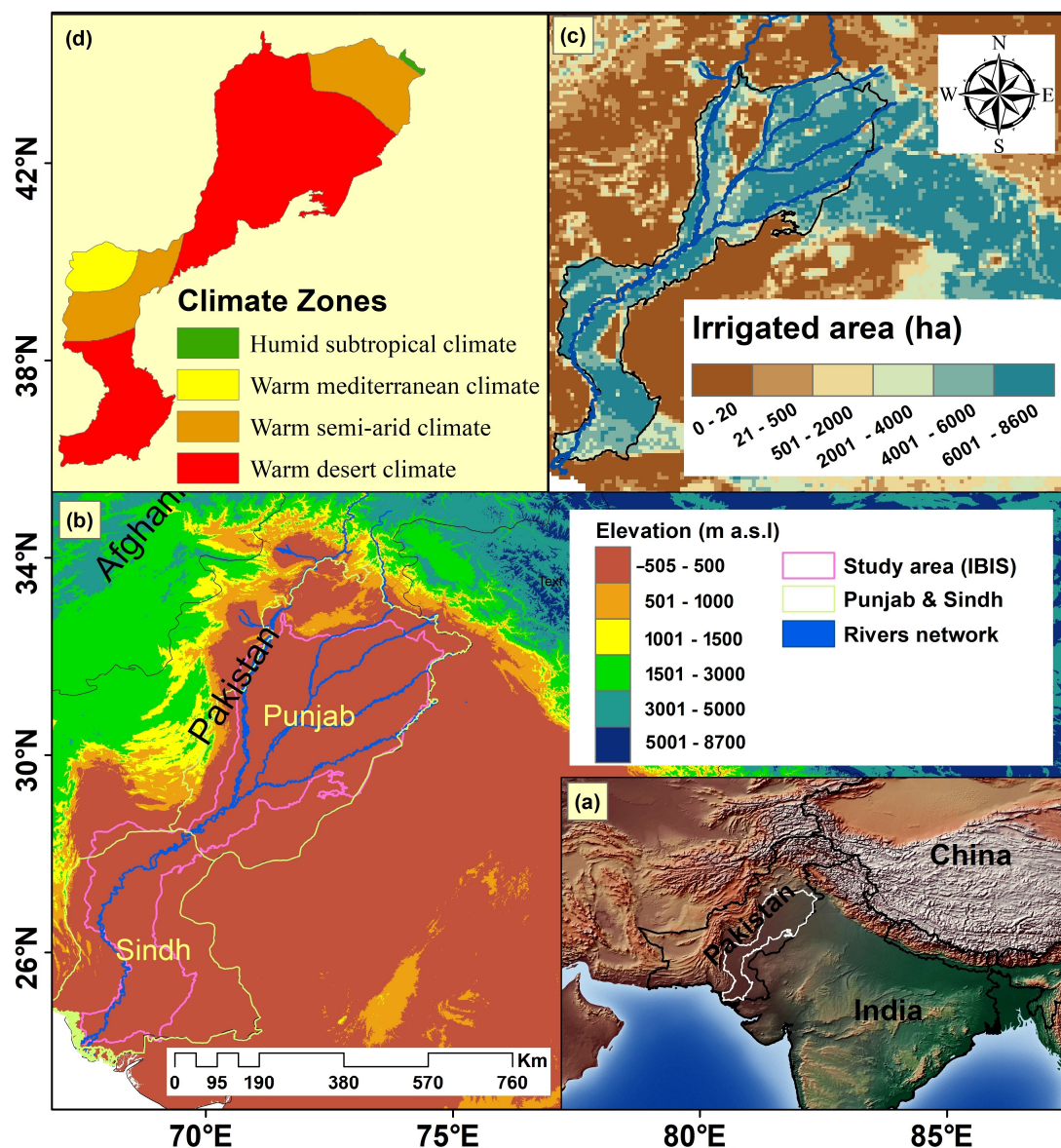


Figure 1. Illustration of the geographic location using the Natural Earth dataset for the IBIS (a) accompanied by the surface elevation (b), the irrigated land area by Siebert et al. [89] (c), and the Koppen Geiger Climate Classification-based climatic zones of the IBIS (d).

Furthermore, the Indus Basin is one of the basins drastically affected by the water sectors due to the progressive increase in population growth, industry, and agricultural development, leading to the over-abstraction of groundwater [71,76]. The IBIS observed semi-arid to arid climatic conditions along with increment in crop water requirements in past years [13,78]. Unfortunately, rainfall and surface water withdrawals have not met the requirement of water demand [90]. Only 30% of the water availability has been observed during the Rabi season varies from November to April, while the rainy Kharif season gives 70% of the available water from May to October [78]. Consequently, a lack of water availability will drastically affect the irrigated agriculture system as agricultural land of approximately 16 million hectares is irrigated through the basin. Therefore, to cope with water scarcity, insight analysis and monitoring of drought are significant. It may assist the water managers in properly managing and planning the water resources and early mitigation system to minimize the intensity and frequency of future droughts.

2.2. GRACE TWSA

The GRACE satellite mission, a collaborated mission between NASA and DLR, measures the Earth's gravitational field to track the variations of total water storage with global coverage. Presently, the GRACE-based gravity records are mainly released from different processing centers, including the German Research Center for Geosciences (GFZ), the Jet Propulsion Laboratory (JPL), and the Center for Space Research at the University of Texas (CSR) with a resolution of $1 \times 1^\circ$ [69,70,78,91]. The GRACE data (RL06, level-3) can be downloaded from (<https://grace.jpl.nasa.gov/data/get-data/>, accessed on 21 June 2020) in units of the equivalent water height, the monthly total water storage data [70,91]. We averaged these three products to have more accurate estimates of TWSA [64,78,87]. Some pre-processing tasks were applied to these data products, including a de-stripping filter, Gaussian smoothing, and glacier isostatic adjustment (GIA) [82]. A GRACE-provided multiplicative scaling factor was applied to restore the original signal lost through data processing [78,87]. For more details on scaling factors, refer to Launderer and Swenson [69]. The data were collected from January 2003 to December 2016, including 20 months of missing data, and all the missing data were filled using linear interpolation [52,71,78,87]. If the data gap occurs during the peak of the wet or dry season, this linear interpolation may (a) underestimate the actual (positive or negative peak) TWSA or (b) it may overestimate or underestimate it if the TWSA experiences significant short-term fluctuations. Furthermore, in areas such as IBIS, which is extremely prone to floods and droughts, these occurrences of overestimation or underestimate could result in inappropriate inferences.

2.3. Precipitation Data

The Tropical Rainfall Measuring Mission (TRMM), a major source of grid precipitation data used in hydrological, ecological, meteorological, and other fields of research [92,93], provides the most commonly used precipitation data at a geographic resolution of $0.25 \times 0.25^\circ$. To match GRACE data resolution, the TRMM data were upscaled to $1 \times 1^\circ$. The TRMM data (Version 7, 3B43) is available from <http://disc.sci.gsfc.nasa.gov/precipitation/>, accessed on 15 May 2020.

2.4. Auxiliary Variables

The Global Land Data Assimilation System (GLDAS) simulates different variables through sophisticated data assimilation models by integrating in-situ observations and satellite data. It makes use of different models such as Noah, Mosaic, Community Land Model (CLM), and Variable Infiltration Capacity (VIC) [94] to simulate a myriad of land surface fluxes, including temperature, precipitation, runoff, soil moisture, evapotranspiration, etc. The Noah model, which has a resolution of 0.25° , was used to derive climatic data, including Potential Evaporation (PEVP), Precipitation (P), Air Temperature (AT), and Specific Humidity (SH) extracted from the Noah model. The Noah model monthly Version 2.1 products exhibited better goodness of fit to GRACE TWS than the other three

models (i.e., CLM, Mosaic, and VIC) [95–97]. Thus, in this study, the GLDAS-2.1 Noah model outputs were applied from 2003 to 2016. GLDAS-2.1 data can be downloaded from <http://disc.sci.gsfc.nasa.gov/hydrology/dataholdings>, accessed on 25 May 2020. Some basic information about the datasets is summarized in Table 1.

Table 1. Concise information on the characteristics of the used data.

Data Type	Variables	Resolution	Units
GRACE (CSR, JPL, GFZ)	TWSA	$1 \times 1^\circ$	mm/month
TRMM	Precipitation (P)	$0.25 \times 0.25^\circ$	mm/month
GLDAS	Soil Moisture Storage (SMS),	$0.25 \times 0.25^\circ$	mm/month
	Canopy Water Storage (CWS),		mm/month
	Surface Runoff (Qs),		mm/month
	Temperature (T),		$^\circ\text{C}/\text{month}$
	Evapotranspiration (ET)		mm/month
Digital Elevation Model (DEM)	Slope, Aspect, and Elevation	90 m	
SPEI	Drought indicator	$0.25 \times 0.25^\circ$	-
Sc-PDSI	Drought indicator	$0.5 \times 0.5^\circ$	-

2.5. Drought Indices

Sc-PDSI is computed using a two-layer soil water balance model driven by different variables such as precipitation, surface runoff, moisture demand/supply, and evapotranspiration [55]. The negative and positive values of the sc-PDSI can determine the wet and dry conditions (<http://www.cru.uea.ac.uk/data>, accessed on 5 June 2020). This index uses the climate-dependent variable input, which makes it able to evaluate the impacts of climate change on drought and climate variations. To validate the WSDI, drought indicators of sc-PDSI and SPEI (<https://spei.csic.es/database.html>, accessed on 10 June 2020) were used. SPEI was chosen for this research based on Penman-Monteith FAO-56, which has potential evapotranspiration data at $0.5 \times 0.5^\circ$ for global regions [53].

3. Methodology

Figure 2 shows this investigation's methodological flow and analytical data structure. Events of drought are identified using the WSD computed from downscaled TWSA. Drought evaluation in the IBIS is attained using the WSDI, developed by standardizing the WSD and then compared with standardized drought indices such as sc-PDSI and SPEI. Additionally, we evaluated inter-annual patterns obtained using the Seasonal and Trend decomposition Loess (STL) method. Total WSD and different levels of drought severity were also examined. Finally, the impact of climate factors was examined using the PLSR model.

3.1. Water Storage Deficit Index Based on Downscaled Data

To detect and describe droughts, the WSDI, which is calculated based on the monthly deviation of downscaled TWSA [46], is calculated as follows (Equations (1) and (2)):

$$WSD_{i,j} = TWSA_{i,j} - \overline{TWSA_j} \quad (1)$$

$$WSDI = \frac{WSD_{i,j} - \bar{x}_{WSD}}{\bar{s}_{WSD}} \quad (2)$$

where $TWSA_{i,j}$ and $WSD_{i,j}$ are the total WSD and downscaled TWSA time series for the j th month in year i , respectively; $\overline{TWSA_j}$ is the long-term mean of TWSA for the equal month (the j th month in a year i), \bar{s}_{WSD} and \bar{x}_{WSD} are the standard deviation and mean of the WSD time series, respectively.

A negative WSD indicates a shortage in total water storage, while a positive WSD indicates a surplus. When a negative WSD persists for three or more consecutive months, a

drought event takes place [46]. Once WSD has been standardized, WSDI may be computed. The WSDI time series represents the monthly departure from the average situation for each month, and its value may be used as a proxy for the severity of the drought.

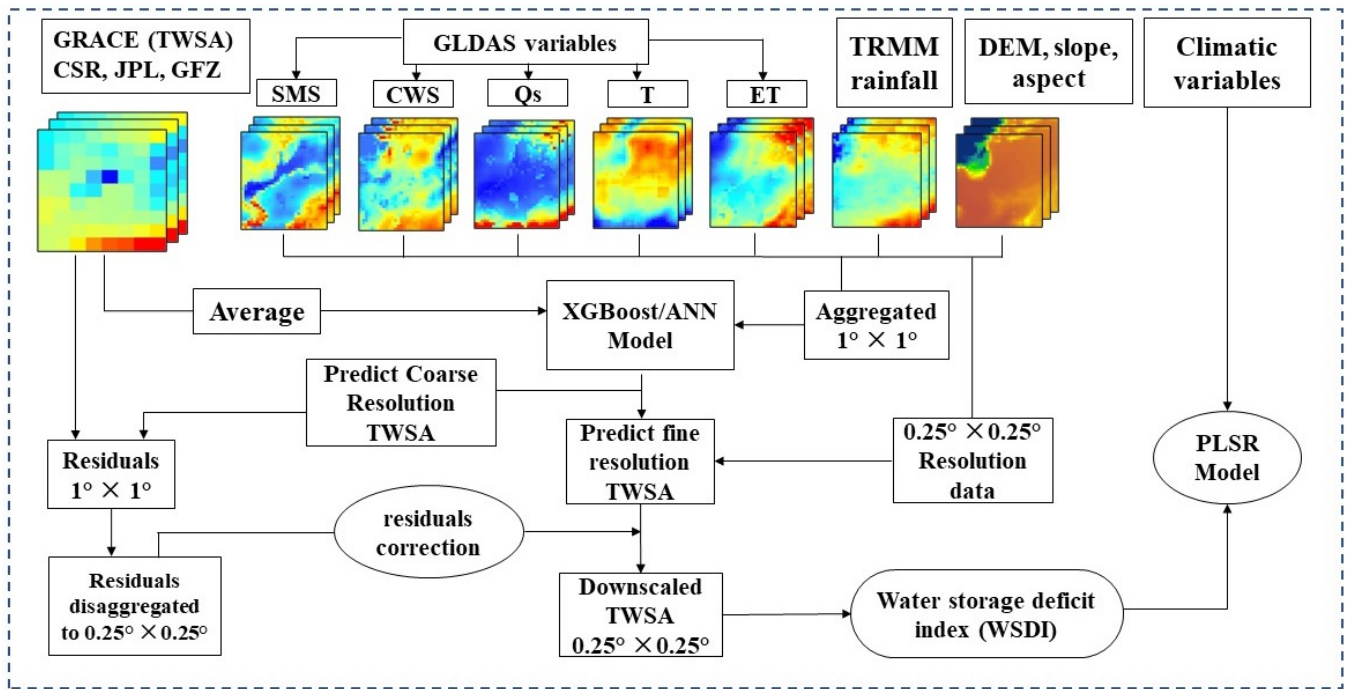


Figure 2. Flow diagram of the downscaling process.

The severity of the drought was assessed using a technique that can account for the combined effects of the deficit in water storage and duration. The following Equation (3) may be used to describe drought events [46]:

$$Se(t) = M(t) \times D(t) \tag{3}$$

where Se stands for “event severity”, “ t ” for “the number of drought events”, which may range from one to many in a particular region, “ M ” for “average deficit since the start of the deficit period”, and “ D ” for “drought event duration”. While the WSDI exposes the relative monthly deficits of water storage over the research period, Se combines WSD with event duration and therefore reflects the total WSD of a certain drought. Total WSD is only a useful signal when a specific drought event has been determined by the WSDI, and the result from the prior month indicates how severe the event was.

Negative values of the WSDI, SPEI, and sc-PDSI indices indicate drought conditions, while the positive values indicate wet periods. The three drought indicators’ magnitudes were used to evaluate the severity of droughts. Table 2 displays the drought severity levels of sc-PDSI [55], SPEI [53], and WSDI [46]. The WSDI data were compared and evaluated using the SPEI and sc-PDSI.

Table 2. The WSDI, SPEI, and sc-PDSI drought categorization.

Grade	Drought Conditions	WSDI	SPEI	Sc-PDSI
D0	No drought	$0 < \text{WSDI}$	$-0.5 < \text{SPEI}$	$-1.0 < \text{Sc-PDSI}$
D1	Mild drought	$-1.0 < \text{WSDI} \leq 0$	$-1.0 < \text{SPEI} \leq -0.5$	$-2.0 < \text{Sc-PDSI} \leq -1.0$
D2	Moderate drought	$-2.0 < \text{WSDI} \leq -1.0$	$-1.5 < \text{SPEI} \leq -1.0$	$-3.0 < \text{Sc-PDSI} \leq -2.0$
D3	Severe drought	$-3.0 < \text{WSDI} \leq -2.0$	$-2.0 < \text{SPEI} \leq -1.5$	$-4.0 < \text{Sc-PDSI} \leq -3.0$
D4	Extreme drought	$\text{WSDI} \leq -3.0$	$-\text{SPEI} \leq -2.0$	$-\text{Sc-PDSI} \leq -4.0$

3.2. Mann–Kendall Test

A nonparametric approach to determining the variation in trend within variables is the Mann–Kendall (MK) test [71,78]. Provided that the values in the time series are independent of one another, the approach has been utilized in research to analyze time series patterns of climatic variables, such as long-term evapotranspiration, precipitation, and runoff. The trend's magnitude may be assessed using Thiel Sen's slope. Positive values indicate an upward trend, whereas negative values indicate a downward trend in this method. Using this approach, it is possible to assess the changes in water storage and the severity of droughts by examining TWSA and drought indices patterns.

3.3. Partial Least Square Regression Model

The Partial Least Squares Regression (PLSR) is a linear regression model to forecast a set of variables from a set of predictors. The PLSR makes predictions by a reduced set of predictor variables, a characteristic that makes it a more efficient tool compared to the standard regression models because the latter fails to work with a large set of variables [98]. The contribution of each hydrometeorological parameter over the IBIS was investigated based on the PLSR model. A dependent variable (Y) can be predicted based on its relationship with a set of independent variables (predictors) (X) through Equation (4):

$$Y = a_0 + a_1X_1 + a_2X_2 + \dots + a_nX_n, n = 1, 2, 3 \dots \quad (4)$$

where a_0 , and a_n denote the intercept and regression coefficient values [99]. The PLSR decides the importance of each predictor on the dependent variable by extracting the data and screening the components [100]. The contribution of each predictor to the predictand variable is quantitatively reported by the variable importance of the projection (VIP) [101]. A VIP of more than 0.8 means that the corresponding predictor can explain the predictand [99]. This study used precipitation, soil moisture, air temperature, potential evaporation, and specific humidity as predictor variables.

3.4. Decomposition of Time Series

The following components of the time series were determined using the nonparametric STL technique through Equation (5) [86,102]:

$$S_{total} = S_{trend} + S_{seasonal} + S_{residuals} \quad (5)$$

where seasonal ($S_{seasonal}$), trend (S_{trend}), and residual components ($S_{residuals}$) are separated from the original signal (S_{total}). For identifying non-linear patterns in trend estimations, the STL technique is based on a locally weighted regression, which is a reliable and computationally effective method. The TWSA time series example is shown in Figure S1. Preliminary studies have used the STL approach to decompose GRACE data and assess inter-annual variability [102–105]. In this study, the inter-annual trends are retrieved from the time series of three drought indicators.

3.5. Machine Learning Models

3.5.1. Extreme Gradient Boosting

As an ensemble learning approach, Extreme Gradient Boosting (XGBoost) is based on the gradient boost tree algorithm. Through the gradient increase technique, residues or mistakes of previous models are anticipated and are added to form the final forecast [106]. The XGBoost must likewise build several decision trees, but each tree must be dependent upon the others, and each new tree must be built on the most recent residuals or errors of the preceding tree. The sum of the values of the leaves in each tree represents the expected value for each sample. Similar to the random forest, XGBoost can accurately manage the multi-collinearity impact and cope with complicated nonlinearity interactions. Multi-collinearity is irrelevant in XGBoost [107,108]. An R package, "XGBoost", was used in R programming [109].

3.5.2. Artificial Neural Network

The ANN generates empirical and non-linear relations between the inputs and the target variable. It develops a network of empirical equations fitted throughout the network learning process to represent these relations quantitatively. A neural network of two-layer feed-forward was employed. The ANN model has three layers: one input layer, two hidden layers, and one output layer. Neurons comprise each layer, which is generated using a back-propagation technique. The propagation method [110,111] is among the widely used methods for supervising the training of multilayer neural networks. The optimal number of hyperparameters in this research was determined via a process of trial and error. The model's performance was assessed using the root mean square error, and the numbers were progressively increased until the anticipated and observed values aligned using the Root Mean Square Error (RMSE). The back-propagation technique iterates through the whole training dataset a specified number of times, or "epochs", in this case. The range of hidden neurons from 100 to 150 and 100 epochs was used in this study to minimize the error value. More details about the neural network and training algorithm are found [112,113]. The precision of the developed models was quantified based on the evaluation metrics applied for the predicted and observed values using the training data.

3.6. Model Design

At first, the XGBoost and ANN models were used to predict the GRACE-derived TWSA at coarse resolution (1°). To create a statistical association between the dependent variable and independent variables at coarse resolution (1°), the XGBoost and ANN models were developed. Resampled to 1° of the independent variables from 0.25° were generated through pixel averaging from 2003 to 2016. Then, these coarse-resolution independent and dependent variables were used to predict TWSA based on the XGBoost, and ANN models. After that, the model with a higher accuracy was selected (XGBoost) and applied to the independent variables at a resolution of 0.25° to attain the predicted TWSA. Subtracting the anticipated TWSA of the XGBoost model from the GRACE-derived TWSA resulted in the computation of the residuals at a resolution of 1°. To obtain the estimated TWSA, the developed XGBoost model was applied to the independent variables at a resolution of 0.25°. The residual correction procedure ultimately resulted in the generation of the final downscaled TWSA values by re-adding interpolated (cubic convolution) residuals (0.25°) to the XGBoost estimated TWSA (0.25°). Figure 2 depicts the downscaling procedure.

3.7. Evaluation Metrics

Model performance was investigated based on four evaluation metrics, including the Pearson correlation coefficient (R), Root Mean Square Error (RMSE), Absolute Error, and Nash–Sutcliffe Efficiency (NSE) through Equations (6)–(9):

$$R = \frac{\sum_{i=1}^n (y_i - \bar{y})(o_i - \bar{o})}{\sqrt{\sum_{i=1}^n (y_i - \bar{y})^2} \sqrt{\sum_{i=1}^n (o_i - \bar{o})^2}} \quad (6)$$

$$RMSE = \sqrt{\frac{\sum_{i=1}^n (o_i - y_i)^2}{n}} \quad (7)$$

$$MAE = \frac{1}{n} \left(\sum_{i=1}^n |y_i - o_i| \right) \quad (8)$$

$$NSE = 1 - \frac{\sum_{i=1}^n (y_i - \bar{y})^2}{\sum_{i=1}^n (o_i - \bar{o})^2} \quad (9)$$

where y and o show predicted and GRACE-derived TWSA values, respectively, n is the length of the time series, \bar{o} and \bar{y} are the mean values of o and y , respectively.

4. Results

4.1. Accuracy Analysis of Machine Learning Models

The input variables were used for training and testing the two machine learning models, and then the TWSA values were simulated. The predicted TWSA was compared to the GRACE-derived TWSA (Figure 3). The results suggest that the XGBoost model outperforms the ANN model with the highest NSE (0.99), R (0.99), RMSE (5.22 mm), and lowest MAE (2.75 mm). Therefore, the XGBoost, satisfying the prediction criteria, can be used as the best model.

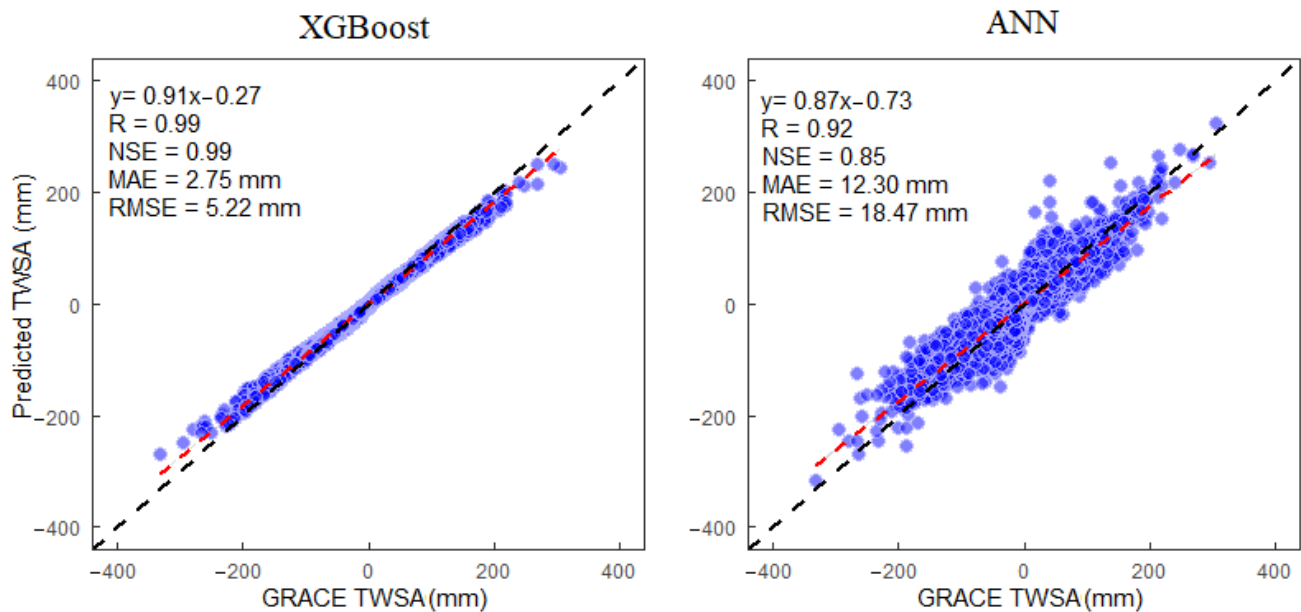


Figure 3. Illustration of machine learning models accuracy in one-one graphs. The dashed black line shows the one-one line and the dashed red line shows the linear trend line.

4.2. Sensitivity Analysis of the XGBoost Model

The significance of the independent variables was further examined in light of the regression model, which evaluated the independent variables' capacity for prediction. The XGBoost-based model's ranking of the relevance of independent variables is shown in Figure 4. Three factors can be identified that significantly affect the fluctuations of TWSA, given the significance of independent variables provided by the XGBoost-based model: DEM, SMS, and precipitation. Precipitation has the greatest impact on changes in TWS [114]. The DEM defines the recharge areas of TWSA as one of the significant influencing elements [115–117]. Another element that affects the TWSA is SMS, which is often used to simulate TWSA [76,78,118–120].

4.3. Analysis of XGBoost Model Performance

4.3.1. Characteristics Analysis of Downscaled TWSA Variation at Spatio-Temporal Scale

The temporal variations of the GRACE-derived and downscaled TWSA (Figure 5) demonstrate a sharp descending trend in the IBIS. Both the downscaled and GRACE TWSA values manifest the same decreasing rate of -3.25 ± 0.45 mm/year at a regional scale. The high association ($R = 0.99$) between the variations of the TWSA trend before and after downscaling indicates that the higher resolution of TWSA can be achieved by the XGBoost model with the highest accuracy. The time series variations of the downscaled and GRACE-derived TWSA verified that the accuracy of the original observations was maintained by downscaling the TWSA.

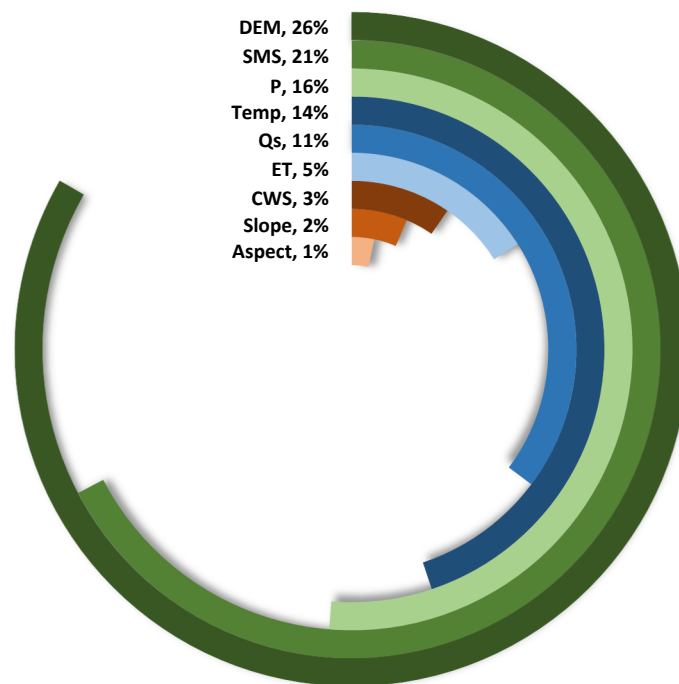


Figure 4. The sensitivity of the XGBoost model to the independent variables in predicting TWSA.

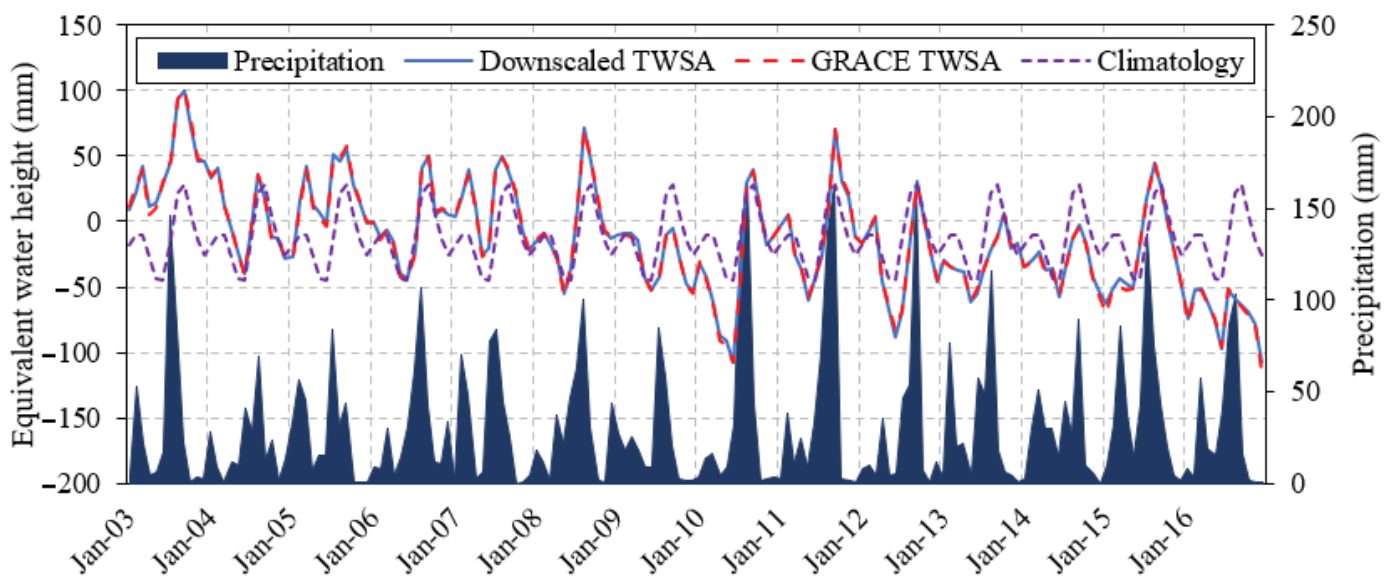


Figure 5. Time series of GRACE-derived and downscaled TWSA, precipitation, and climatology.

The climatology for 168 months was calculated using the downscaled TWSA time series from January 2003 to December 2016 by averaging the data of each month (from January to December) (Figure 5). The climatology serves as a basis for determining the severity of water storage deficits and frequency and illustrates the typical fluctuation of water storage. By doing so, we may describe unique events that diverge from the regular annual cycle and take into consideration geographical areas with weak or high seasonality. We understand that a climatology of at least 30 years is ideal [46], but for the time being, the GRACE mission's consistent water storage with worldwide coverage is the best option.

It can be observed from Figure 5 that the maximum TWSA depletion happened in June 2010 (-107.22 mm/month) and December 2016 (-106.98 mm/month). Therefore, for instance, downscaled TWS variations were analyzed at the spatial scale for June 2010 (Figure 6). More details of the TWSA variations on the spatial domain were observed for the downscaled TWSA than for the GRACE-derived TWSA. Spatially, the overall

trends of the original and downscaled TWSA are similar. The TWSA declined over the region of the study area (IBIS) but decreased more in the middle of the IBIS. The TWSA manifests more effective spatial variability after downscaling. The spatial variations of the downscaled TWSA efficiently represent the sub-grid heterogeneity of the TWSA that occurred mainly due to the impacts of hydroclimatic and geospatial variables at the local scale. The downscaled TWSA's geographical distribution maps throughout the research region displayed the same trends as the GRACE-based TWSA.

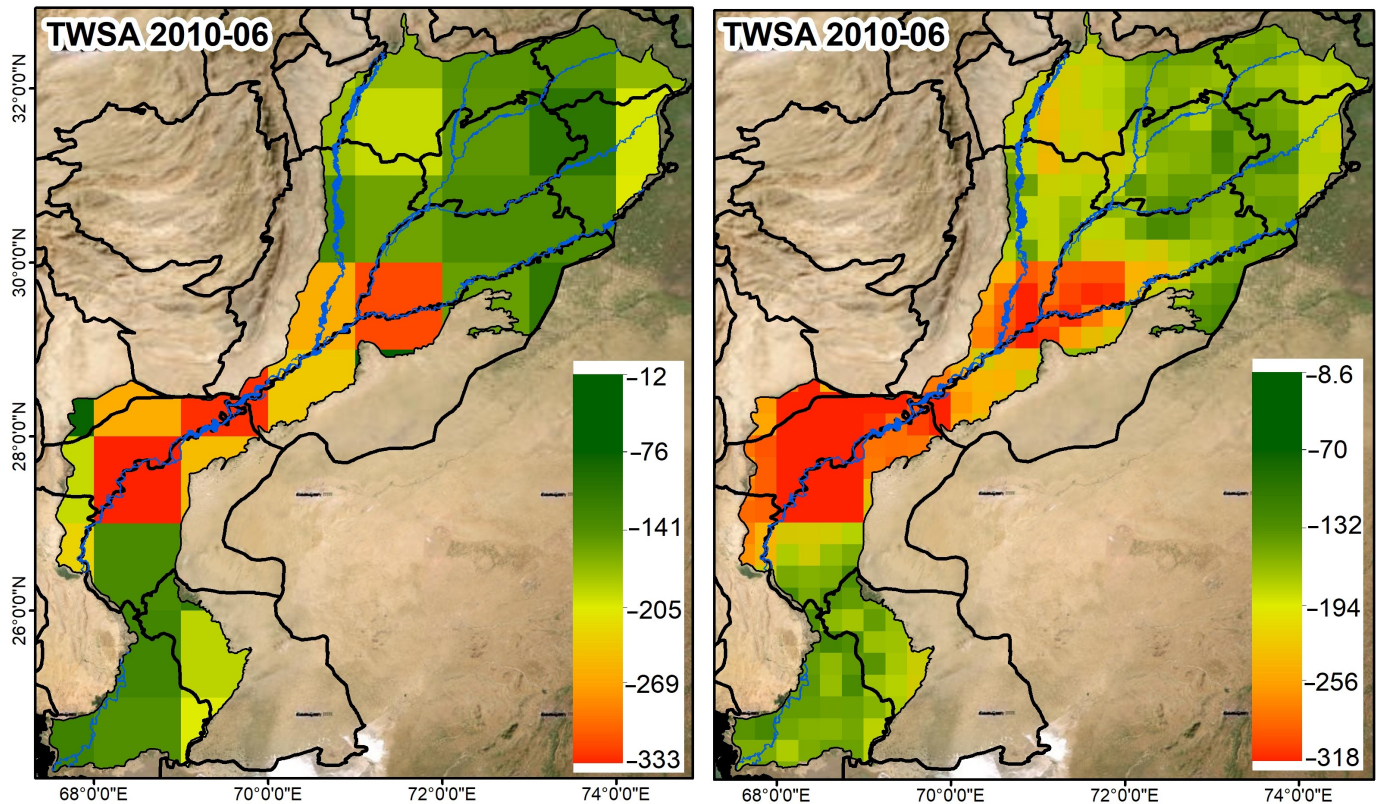


Figure 6. TWSA (mm) spatial changes before (left) and after (right) downscaling in June 2010.

4.3.2. Estimation of Terrestrial Water Storage Deficits

The properties of TWSA are influenced by variations in precipitation. The monthly precipitation anomaly (PA) was generated using the long-term mean (2004–2009) similar to the GRACE TWSA data, and it is used to compare with downscaled TWSA as anomaly values. Figure 7a displays the downscaled TWSA and PA time series. It was clear that from 2003 to 2016, the monsoon season was when precipitation was at its highest. The data showed that the most notable summer rainfall occurred in 2010 and 2011 and that these times coincided with the maxima in downscaled TWSA time series. The rainfall increased somewhat less dramatically, at a rate of 0.46 mm/year, compared to downscaled TWSA, which declined at a rate of -3.25 mm/year between 2003 and 2016.

The deficit in TWSA is a significant indicator of drought manifestation. Figure 7b displays the cumulative WSD and temporal variations in WSD from 2003 to 2016. In 2010 and 2016, there were significant water storage deficits (Figure 7b). More precisely, in June 2010 and September 2016, respectively, deficits of -61.97 mm and -92.06 mm were found. The water storage was mostly in deficit in subsequent years, except in 2011 and 2015, clearly showing a surplus, with peaks of 32.82 mm in November 2011 and 29.16 mm in July 2015. Figure 7b clearly illustrates the transition from a WSD surplus to a deficit, which occurred roughly in 2009/2010. In 2009, the WSD trend started to decline after a prolonged increase. A consistent surplus in water storage was present from January 2003 to May 2009, while a consistent deficit was observed from June 2009 to December 2016. A persistent water

storage deficit is shown by a declining trend, while a persistent water storage surplus is indicated by an increasing trend.

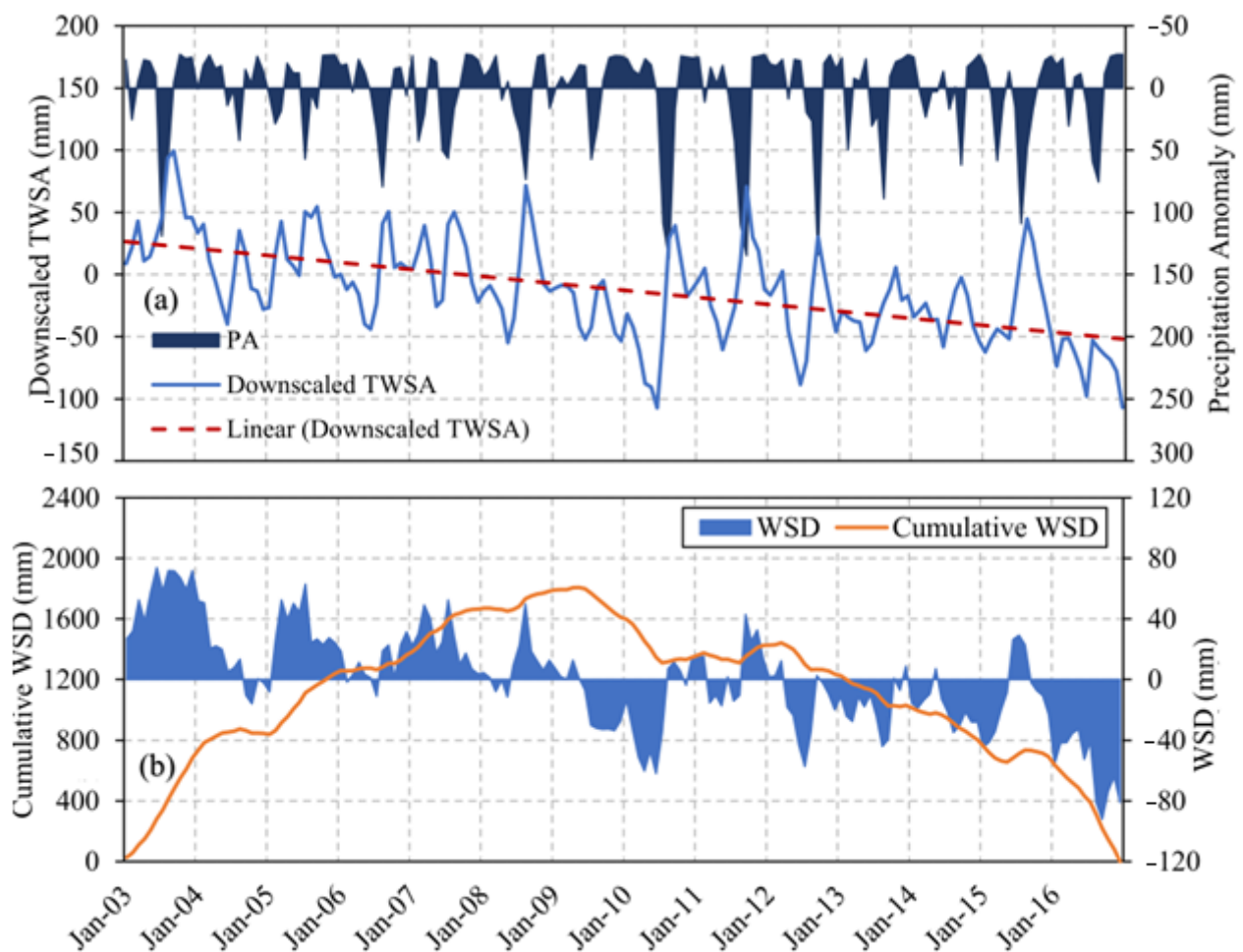


Figure 7. (a) Time series of downscaled TWSA and precipitation anomaly (PA) and (b) water storage deficit (WSD) and cumulative WSD for the IBIS.

Eight droughts were identified in the IBIS between 2003 and 2016 following the criteria of a drought event [46] (Table 2). The two longest drought periods in the area were from June 2009 to July 2010 and September 2015 to December 2016, lasting 14 and 16 months, respectively. Peak deficits were measured in June 2010 and September 2016 with magnitudes of -61.97 mm and -92.06 mm, respectively. In addition, the high relative peak deficit (-92.06 mm) recorded in September 2016 and the high total WSD (-734.01 mm) made the drought event (September 2015 to December 2016) the most severe one.

Figure 8 shows the averaged monthly variations of GRACE and downscaled TWSA and precipitation from 2003 to 2016. Generally, the TWSA follows the trend of increasing and decreasing, similar to precipitation. The TWSA has an increasing and decreasing trend from January to May, gradually increasing during the monsoon season (June–September), and decreasing from October to December in IBIS (Figure 8a). The variations in precipitation also show an almost similar increasing and decreasing pattern to TWSA (Figure 8b). It indicates that precipitation is an important factor in impacting the variations of downscaled TWSA. Precipitation is an essential source of water that influences the variation in water storage. Accordingly, these findings suggest that climatic variability may impact the water storage deficit [105].

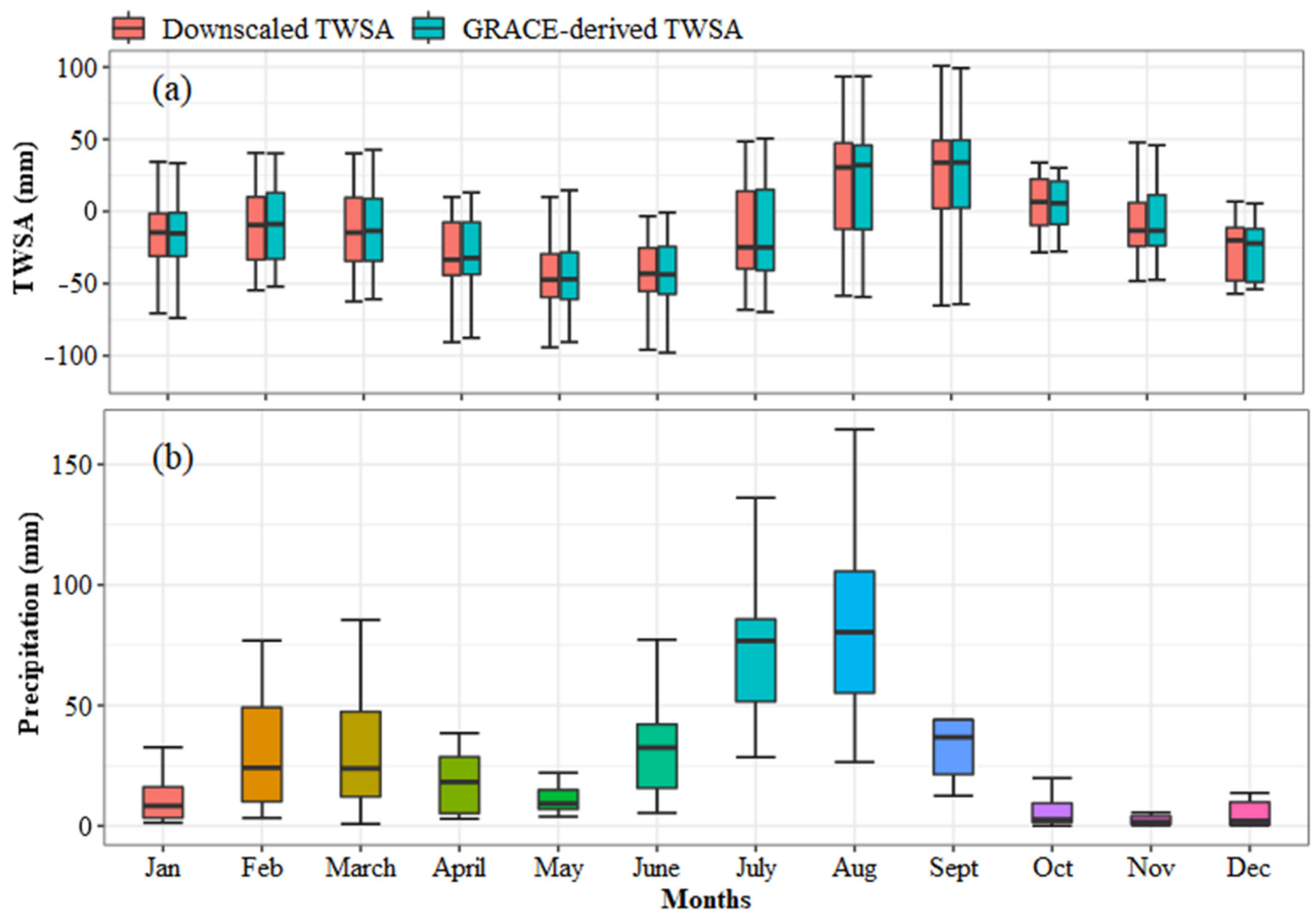


Figure 8. Box plots showing (a) the monthly distribution of GRACE and downscaled TWSA and (b) precipitation in the IBIS from 2003 to 2016.

4.3.3. WSDI Comparison with Other Drought Indices

Generally, with identical peaks and troughs, the WSDI's behavior and response to the climatic irregularities were in good agreement with those of the other indices (Figure 9a). Consistent features could also be seen in the corresponding inter-annual patterns revealed using the STL decomposition (Figure 9b). However, given that these indices are developed using various factors and approaches, certain variations in their behavior were also noted [30]. For instance, WSDI usually fluctuated between higher and lower levels than the other indices, except for the years 2009 and 2010 (Figure 9b), supporting the findings in Figure 7b that this time frame represents the turning point for WSD. When compared to other drought indicators, the sc-PDSI had the biggest peaks and falls (Figure 9b). When the overall WSD was second-most significant in 2009 and 2010, all drought indicators showed the same largest declines. The drought indices are more consistent between 2009 and 2010. Therefore, in the next section, we discussed the spatial distribution of drought based on downscaled TWSA only during 2009–2010.

4.3.4. Distribution of Drought at the Spatial Scale

The initiation and termination of the drought episodes from June 2009 to August 2010 are also reflected in the geographical distribution of drought as determined by the WSDI (Figure 10). The findings show that severe and extreme droughts completely cover the IBIS during the drought episodes. The area-mean monthly values of the WSDI over the study area from 2009.06 to 2010.08 were -0.23 , -0.87 , -0.89 , -0.92 , -0.95 , -0.96 , -0.78 , -0.40 , -0.92 , -1.34 , -1.64 , -1.29 , -1.71 , -0.95 , and 0.17 , respectively. The largest drought, with

a WSDI value of -1.71 , occurred in June 2010, affecting nearly entirely IBIS. In August 2010, the drought relief was significant, with a WSDI score maximum value of 0.07 . Thus, taking suitable drought-resilient measures over the IBIS is mandatory to alleviate the harsh side effects of drought events and to boost the capacity for drought resistance. In addition, spatial patterns of downscaled TWSA are given in Figure S2 from June 2009 to August 2010 for the IBIS.

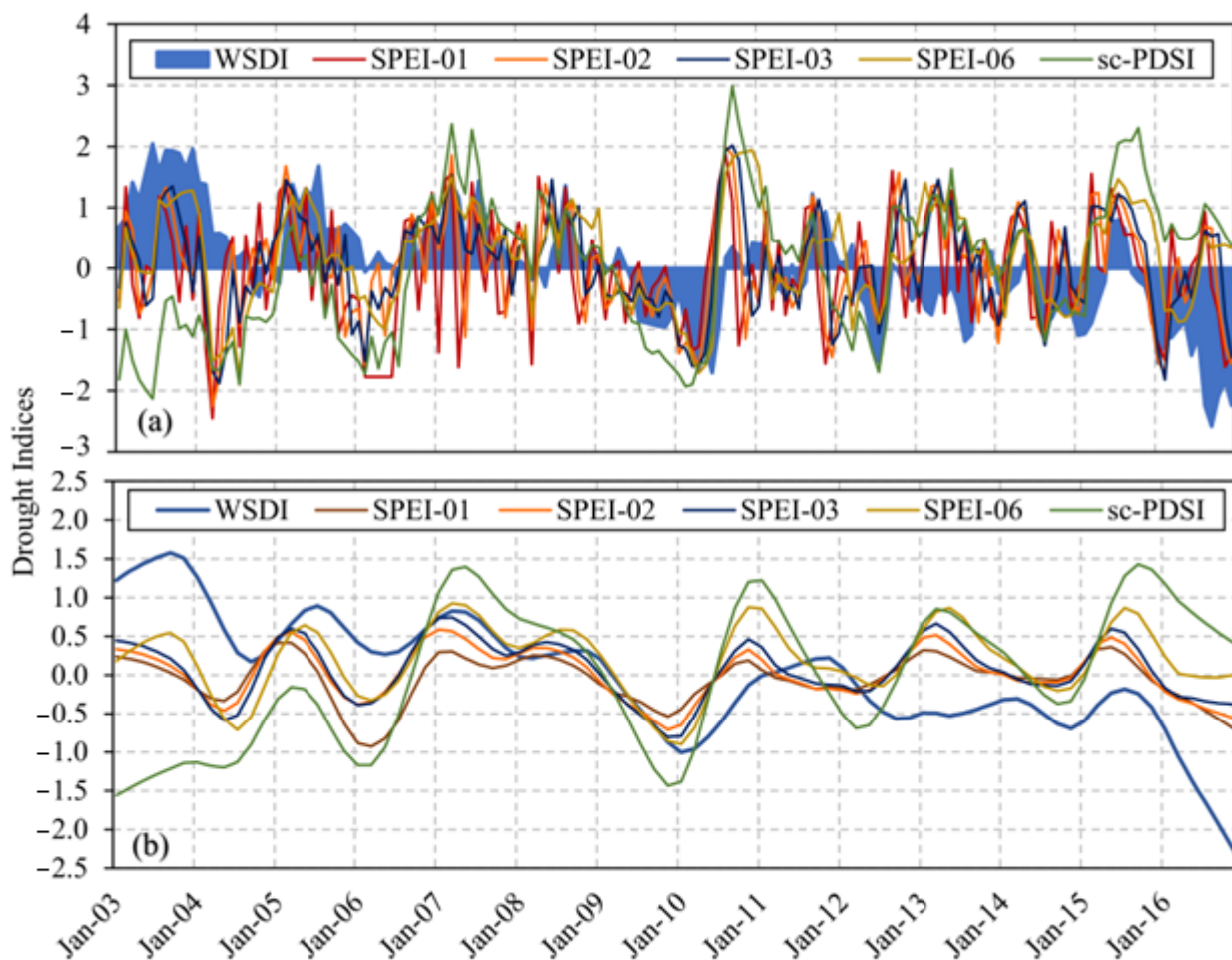


Figure 9. (a) WSDI comparisons with other drought indices and (b) STL decomposed inter-annual trends for the IBIS.

4.3.5. The Associations between Climate Factors and WSDI

To better understand the causes and formation of drought due to climate change, it is vital to investigate the association between drought and climatic parameters. The PLSR model was used in this work to mimic the relationships between climatic variables and drought. Based on the VIP produced from the PLSR model, the influence of numerous climatic variables on the emergence of the drought was assessed. The results of decomposing both climatic components and WSDI using the STL to extract the inter-annual trend before using the PLSR model are shown in (Figure S3).

With a determination coefficient (R^2) of 0.80 and high goodness of fit, the PLSR model-based simulation result shows that climatic conditions are the main cause of drought in the IBIS. As shown in Figure 11, P (1.45), PEVP (1.42), and SMS (0.93) have VIP values larger than 0.8 , whereas AT and SH have lower VIPs with values of 0.11 and 0.03 , respectively. The PLSR model can successfully pinpoint the relationships between drought and climatic conditions in conclusion. Inadequate precipitation is the primary cause of drought, followed by significant potential evaporation in the IBIS from 2003 to 2016.

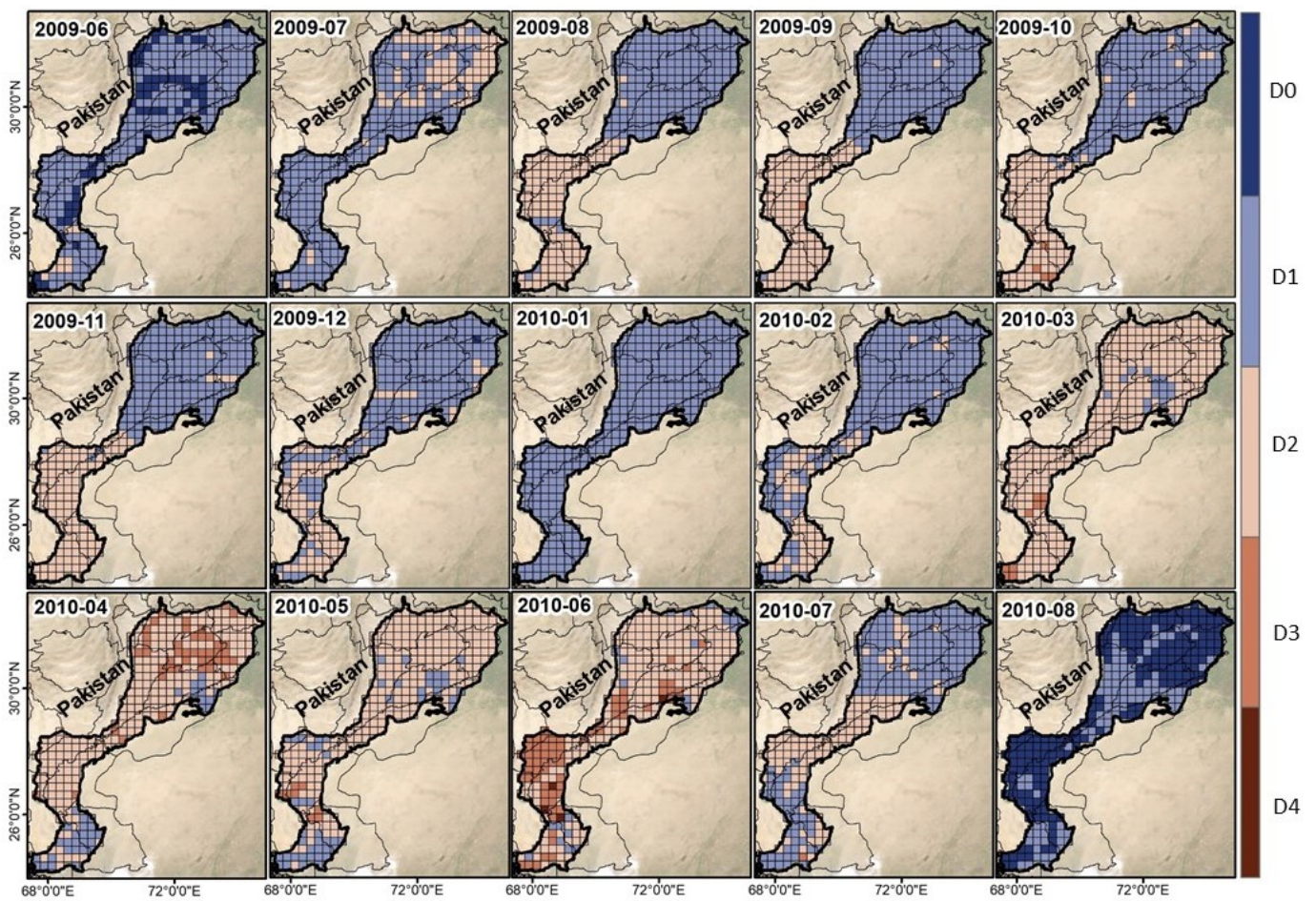


Figure 10. Drought events were captured from June 2009 to August 2010 at a spatial scale in IBIS.

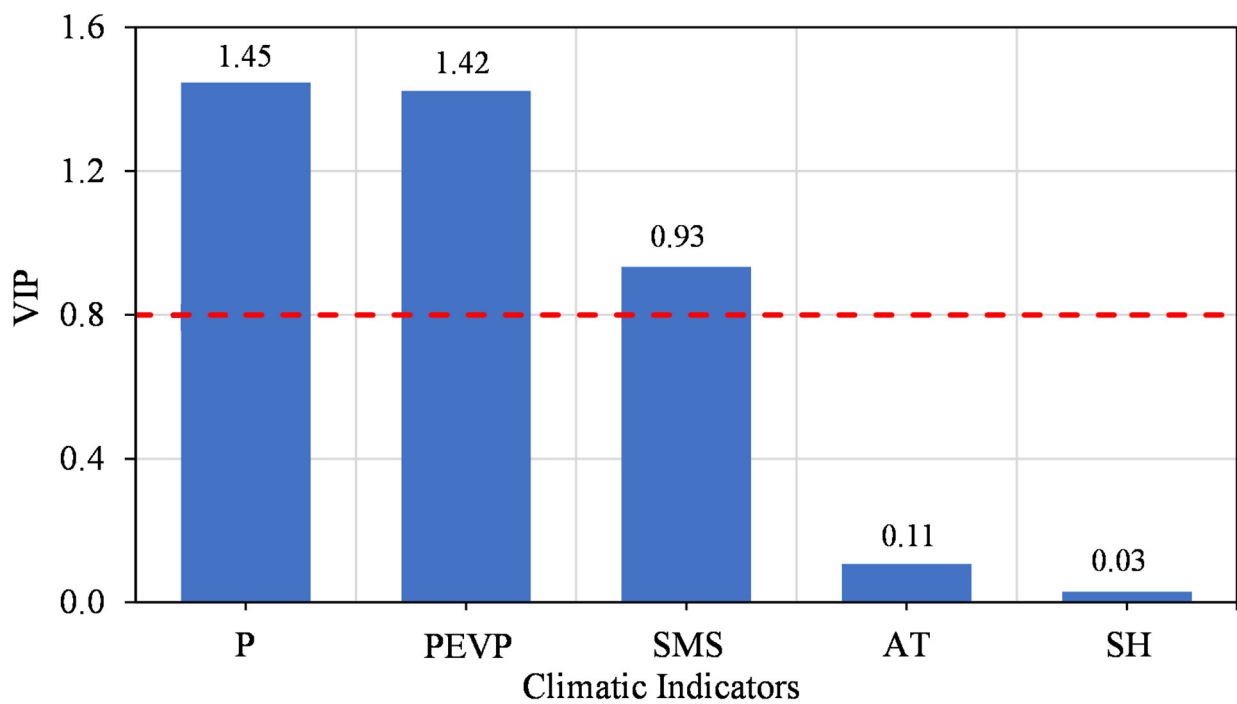


Figure 11. The effect of several climatic indicators on drought from 2003 to 2016 is based on the PLSR model.

4.3.6. Drought Events Detected by WSD

Figure 12 depicts the general severity of drought on a specific time scale throughout the IBIS from 2003 to 2016. The severity values are represented along with each of the drought events to more accurately examine and compute the drought intensity across the study duration (Figure 12).

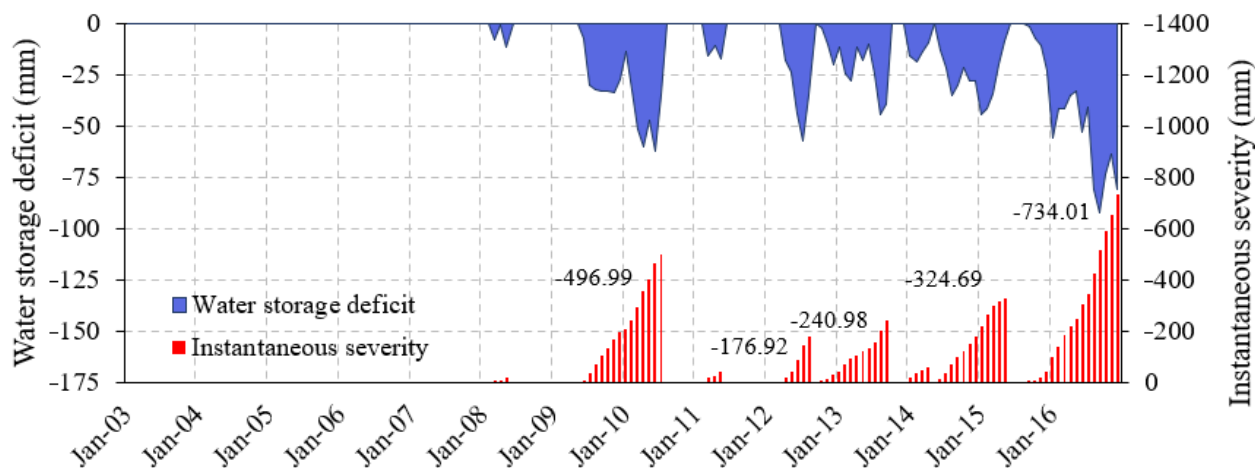


Figure 12. Water storage deficit and instantaneous severity values for the downscaled TWSA data and corresponding overall drought severity values.

In this graph, droughts of greater severity are represented by higher WSD and longer durations. The drought events that occurred in 2010 and 2016 were the most prolonged deficit periods, lasting 14 and 16 months, respectively, out of the eight drought events that were detected throughout the IBIS during the research period. The overall hydrological severity of these two droughts, -496.99 mm and -734.01 mm, respectively, was likewise the greatest. The seventh drought episode, which had a severity of -324.69 mm and lasted for 12 months, occurred between June 2014 and May 2015. This event was ranked third in terms of its length and intensity. Several more minor droughts or temporary droughts also occurred throughout the research period (Table 3).

Table 3. A summary of the detected drought events based on the downscaled TWSA.

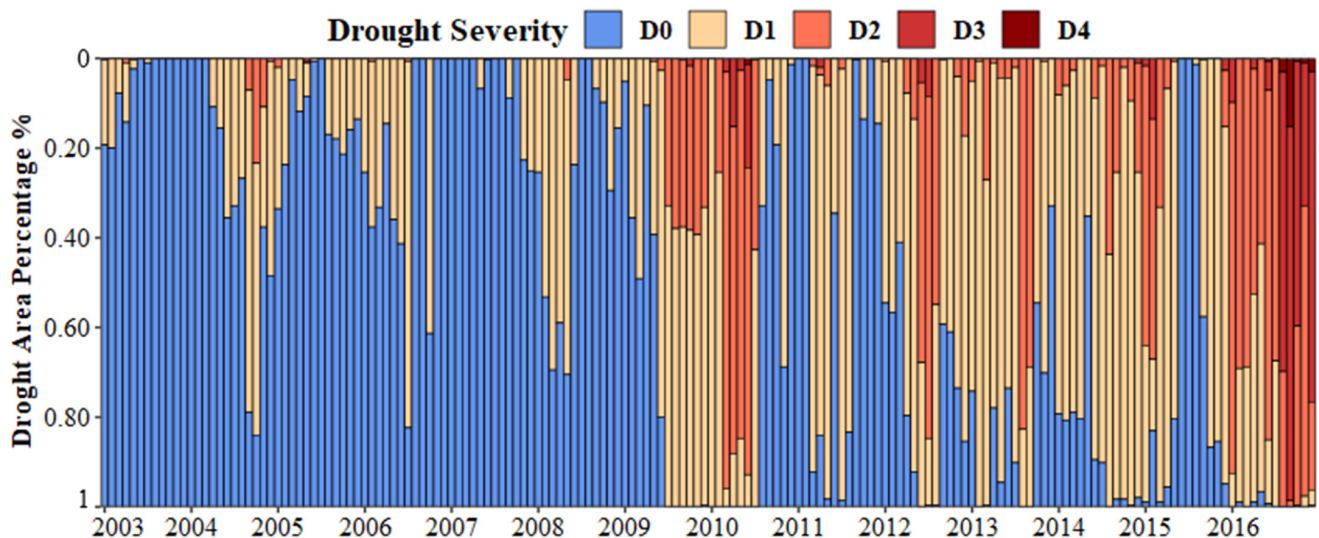
Period	Duration (Month)	Total Severity (mm)	Average Deficit (mm)	Peak Deficit (mm)
March–May 2003	3	−19.47	−6.49	−11.35
June 2009–July 2010	14	−496.99	−35.50	−61.97
March–May 2011	3	−42.86	−14.29	−17.10
April–August 2012	5	−176.92	−35.38	−57.31
October 2012–September 2013	12	−240.98	−20.08	−44.10
January–April 2014	4	−57.14	−14.29	−18.57
June 2014–May 2015	12	−324.69	−27.06	−44.13
September 2015–December 2016	16	−734.01	−45.88	−92.06

When describing the severity of the drought, drought indices are often categorized into several levels. There are noticeable differences in the severity of drought according to different drought indices for the same drought episodes (Tables 2 and 4). For instance, the WSDI classifies drought events No. 2 and 8 as moderate droughts (D2), but SPEI-01, -02, -03, and sc-PDSI classify event No. 2 as no drought (D0) and mild drought (D1), respectively. Event No. 8 is also categorized as a no drought (D0) based on SPEI-01, -02, -03, and sc-PDSI. Overall, however, it is evident that there were noticeable differences in the levels of drought severity of the eight drought episodes recognized by these drought metrics.

Table 4. Drought severity categories are based on several drought indicators.

Period	WSDI/ Category	SPEI-01/ Category	SPEI-02/ Category	SPEI-03/ Category	SPEI-06/ Category	Sc-PDSI/ Category
March–May 2003	−0.17/D1	0.22/D0	0.19/D0	−0.02/D0	−0.02/D0	0.76/D0
June 2009–July 2010	−1.00/D2	−0.34/D0	−0.56/D1	−0.70/D1	−0.84/D1	−1.27/D1
March–May 2011	−0.40/D1	−0.33/D0	−0.11/D0	−0.17/D0	−0.31/D0	0.38/D0
April–August 2012	−0.95/D1	−0.11/D1	−0.28/D1	−0.30/D1	−0.48/D1	−1.14/D1
October 2012–September 2013	−0.56/D1	0.18/D0	0.56/D0	0.65/D0	0.78/D0	0.84/D0
January–April 2014	−0.35/D1	0.27/D0	0.07/D0	−0.03/D0	−0.01/D0	0.19/D0
June 2014–May 2015	−0.71/D1	−0.10/D0	−0.07/D0	−0.04/D0	−0.09/D0	−0.27/D0
September 2015–December 2016	−1.28/D2	−0.38/D0	−0.36/D0	−0.24/D0	0.16/D0	0.94/D0

An alternate method may be used to evaluate the severity of drought in the regions impacted by different drought levels. The geographic dispersion of the drought-affected regions illustrates how the drought develops and the regions that experience drought of various intensities. Figure 13 displays a sample geographical distribution of WSDI. The percentage area subjected to the monthly droughts of various severity levels is shown in Figure 13. Drought events occurred in June 2009–July 2010 and September 2015–December 2016, affecting 52% of the IBIS with a mild drought (D1), 46% with a moderate drought (D2), 9% with severe drought (D3), 1% with extreme drought (D4), and 40% with a mild drought (D1), 48% with a moderate drought (D2), 37% with severe drought (D3), and 4% with extreme drought (D4), respectively, were the two drought events that affected. Most IBIS generally endures moderate drought, with rare severe drought.

**Figure 13.** The percentage of the area subjected to droughts of varying severity from 2003 to 2016 (D0: no drought; D1: mild drought; D2: moderate drought; D3: severe drought; D4: extreme drought).

5. Discussions

5.1. Factors Influencing Drought

Accurate research of the components that influence drought is crucial to fully comprehending drought management because of accelerated global climate change [121]. The most important elements contributing to drought in the IBIS are the irregularity in precipitation and the rise in potential evaporation [101] based on the PLSR model. Insufficient water supply will result from a lack of precipitation, which will directly hamper human and plant development. Furthermore, high potential evaporation will also disturb the balance of the water cycle and speed up the loss of available water resources [122]. Additionally, the WSDI and climatic indicators yearly trends are extracted using the STL approach, and their comparison reveals the link between them. Figure S4 shows the unusual decline

in precipitation and rise in potential evaporation during drought duration between June 2009–July 2010 and September 2015–December 2016, further demonstrating the reliability of the simulation findings from the PLSR model.

5.2. The Sources of Uncertainties

Several uncertainty sources were involved in this study. Firstly, to diminish the uncertainties ascribed to the GRACE data, we applied an ensemble mean of three GRACE spherical harmonic solutions [71,78,87,123]. In addition, various hydrological models were taken into account by the spherical harmonic coefficient solutions to alter the scale factor, which ultimately adds to the existence of uncertainty. Second, the ensemble means of the GLDAS models (VIC, Noah, Mosaic, and CLM) were proposed to reduce the GLDAS uncertainty [124]. However, only the Noah model has a similar spatial resolution (0.25°) as the XGBoost-based downscaled TWSA. Therefore, to decrease the uncertainty associated with spatial resolution while analyzing water storage estimations, we utilized the GLDAS-2.1 Noah model results in the current research. Thirdly, the ensemble-based approach of machine learning models may appropriately decrease the uncertainty associated with the machine learning models used to predict the higher resolution of the TWSA [125]. Finally, using linear interpolation to fill in missing gaps in GRACE data would also trigger uncertainties in the assessment. Although this approach to handling missing data is reliable, prevalent, and frequently used [51,78,105,126,127], the missing data may also be filled in using other TWSA time series construction methods, for example, an artificial neural network (ANN) model [128,129].

5.3. Evaluation of Water Storage Deficit

A huge water deficit often shows a drought episode with greater severity. The IBIS became drier from 2003 to 2016, as shown by the declining trend of TWSA (Figure 5). The impacts of climate change are most likely to be responsible for this decline. Positive WSD before 2009/2010 and negative WSD after 2009/2010 (Figure 7b) may indicate an increase in droughts' frequency or severity. Given that the cumulative WSD was drastically declining in 2009, it was more evidence that this was the year when the water storage went from being in excess to the deficit (Figure 7b). Despite an overall decline in the total WSD from 2009 to 2016, this period also includes drought events Nos. 2 through to No. 8. The WSD based on downscaled TWSA generally recognized drought events that agreed with other drought indices from 2009 to 2010 for the IBIS.

5.4. Analysis of SPEI, sc-PDSI, and WSDI

Standardized WSD is used to better indicate the severity of droughts as well as to compare WSDI with other standardized drought indicators. The magnitude of a water deficit may be determined using WSD, but it is unable to reveal how severe the drought was in various geographic locations. In general, the WSDI's behavior and response to climatic deviations were in reasonable agreement with other indicators studied in this research (Figure 9). Because the other drought indicators are generated based on diversified algorithms and techniques, discrepancies in behavior across different drought metrics are unavoidable. While the sc-PDSI is based on the potential values of the variables, i.e., the highest possible values of each variable, the SPEI makes use of precipitation and evapotranspiration, which is more likely to overstate the hydrologic situations [105]. Moreover, these conventional drought indicators rely on climatic variables and hydrologic fluxes that only contribute a small amount to the top surface. In contrast, variations in the subsurface may also be crucial in the development of drought, particularly for long-lasting and extremely severe drought events. By combining the impacts of numerous surface and subsurface hydrologic processes, WSDI, on the other hand, can determine the precise quantity of water that is lost from storage. Consequently, it is anticipated that this index will be more effective in illuminating the actual hydrological conditions in a given area and the underlying internal dynamics of drought development. Furthermore, the spatial properties

of the involved regions in an area of interest may not be correctly described by the point data acquired from meteorological and hydrological stations. For large-scale regions, this is particularly true. WSDI offers a more logical approach than previous drought indices since its mathematical and statistical calculations are less complex [105]. WSDI offers a massive range of potential applications, particularly in regions of large scale and areas with insufficient stations for hydrometeorological data. WSDI, however, is also linked to several limitations. The area-mean monthly water storage is not accurate enough for short TWS time series, according to the assumption of Thomas et al. [46] that a minimum of 30-year time series is optimal, making the calculation and evaluation of droughts using WSDI difficult. The additional records may be added to the time series to calculate improved WSDI, enabling ongoing updates to this approach as the GRACE record grows over time.

5.5. Drought Severity Evaluation

Terrestrial hydrological conditions and climatic anomalies are key factors in determining the severity of a drought. Various drought indicators are used to determine different drought levels (Table 4). The current results showed that there were differences between the categories of drought indices. The observed variations and discrepancies in the findings might be attributable to the fundamentally diverse data types, calculation techniques, and time scales utilized to calculate the various indices [105].

Previously, Thomas et al. [46] used total WSD during the occurrence of drought to estimate the drought severity. WSD is based on the monthly peaks in estimating the drought severity and thus is different from this approach. Hypothetically, using total WSD to assess the severity of drought is more practically significant than using the monthly peak deficit. Subsequently, the overall deficit amount may represent general water deficiencies linked with drought and can, hence, more clearly identify the severity of drought. However, it may be difficult to determine precisely when a drought starts and ends. As a result, a drought event is sometimes not recognized until its destructive impacts start to affect a specific area [130,131]. According to the methodology described by Thomas et al. [46], a drought episode is one in which the WSD persists for three or more months in a row. It should be highlighted that there is generally good agreement between the drought severities determined by these two methodologies, as shown by the severity of eight drought events that were the focus of the current investigation (Figure S5). A more severe drought is indicated by large WSD and low WSDI readings, and vice versa. The 2010 and 2016 drought occurrences were the two most severe droughts evaluated in this investigation between 2003 and 2016, followed by the 2013 and 2015 droughts (Figure 12).

Categories for drought severity often correspond to WSD levels. It is essential to measure the severity of the drought in terms of its extent due to the area percentages impacted by the different degrees of drought (Figure 13). It was also found that drought episodes impacted the biggest area in 2010 and 2016 (i.e., the combined area affected by droughts of different severities). The extent of the 2010 drought showed that mild and moderate drought hit a wider region than usual. In the IBIS, severe and moderate drought conditions impacted a maximum area percentage of 54% as of June 2010 (Figure 13). More specific information about this drought may also be determined by finding the region that is affected each month by droughts of different levels of severity.

5.6. Comparison to Previously Related Studies

The lost data of the GRACE mission was filled in through interpolation. This process induces uncertainties in the estimated TWSA. To evade these errors, as a more accurate approach, an Artificial Neural Network (ANN) could be utilized in future research to fill in data of missing months. In recent times, Gemitzi and Lakshmi [77] and Miro et al. [132] downscaled the GRACE data using the ANN model. Although the calibration of the first model showed overestimated in-situ data, the overall performance of both models was good. The other model [132] suggested an error of almost 1 m in some regions in comparison to the observed data. Meanwhile, Seyoum and Milewski [123] performed an ANN model

to simulate variables by considering the data lags. The data of this model exhibit weak Pearson's correlation coefficients by depicting more variations than observed. Reference [90] developed an ANN model to downscale GRACE data. The model-based GWS yielded a Pearson's correlation coefficient of 0.64, along with an RMSE of 22.50 mm [78,82,84] used RF and ANN models for downscaling the GRACE TWSA and reported the correlation ranging from 0.83 to 0.97 and RMSE ranging from 11.83 to 53.75 mm. This study suggests the XGBoost for downscaling GRACE data, and its outputs show a strong correlation coefficient when compared to the ANN model and an RMSE of 5.22 mm (Figure 3). It effectively enables the examination of TWSA in more detail at a small regional scale after improving the resolution of GRACE data.

5.7. Advantages and Limitations

The GRACE data contribute substantially to drought assessment in places with limited water storage data [133]. Different filtering methods can be applied to diminish the impacts of errors in the gridded GRACE-SH data, yet results indicate the possibility of weak signals in the derived product. Therefore, scale factors are applied to restore signal leakage induced by the filtering process [69]. The GRACE data are critical to drought analysis in regions with limited hydrometeorological data. The current study assessed drought characteristics based on the WSDI metric. It is a standardized index that offers strong evidence for investigating surplus and deficit terrestrial water availability [46]. The drought incidents between June 2009 and August 2010 were positively established in this study. The results of the study suggest that by using the GRACE estimates, one can efficiently describe drought characteristics. However, it seems that there is a specific limitation in this study. For a more accurate characterization and detection of droughts, a longer record of GRACE data is required [46]. With the accuracy of tens of millimeters of equal thickness and global coverage, the GRACE is a unique technology for the accurate monitoring of terrestrial hydrology. It provides realistic spatiotemporal variations in water storage components. With an opportunity of having access to the extended data from the GRACE Follow-On (GRACE-FO) satellite datasets, the long-running evaluation of TWSA variations and their associated droughts will be possible. Using cubic convolution interpolation, the TWSA's coarse residuals were resampled, and additional consideration of the inter-pixel variations is needed. The IBIS is short of accurate data on surface water storage, such as lakes, rivers, and reservoirs; thus, we ignored the contributions of these sources. Moreover, the lack of observations on the anthropogenic forces and difficulties in collecting and measuring relevant information forces the researchers to ignore their influence on the Earth's mass changes [134]. As a result, these factors should also be considered while analyzing droughts, which could offer new scientific insights in the future. However, the downscaled TWSA data we have generated can offer some guidance for in-depth studies of the regional TWSA and can help advance future hydrological research, improving the capabilities for sustainable water resources management.

6. Conclusions

Concerning large-scale water storage depletion and droughts, GRACE satellite data has been very insightful for the study of hydrology. We assessed the drought events that occurred in the IBIS from 2003 to 2016 based on the downscaled TWSA data and standardized the WSD to produce WSDI. It is then utilized to assess and define all detected drought events. Additionally, discrepancies were analyzed and explained in the drought categories based on total WSD and WSDI, as well as presented a thorough comparison of WSDI with other recognized drought indices, including the sc-PDSI and SPEI. The results demonstrated that the IBIS became drier over the research period. Based on the WSD, the eight drought episodes were determined dominantly. The two most severe drought episodes, with WSDI of -1.20 and -1.28 and total WSD of -496.99 mm and -734.01 mm, respectively, occurred in 2010 and 2016. Based on different drought indicators, drought events were categorized into various drought severity levels. These results may be

explained by variations in the calculation of data and methods, time scales, and category criteria of the used indices. In general, the WSDI values of -1.00 and -1.28 for the drought events of 2010 and 2016 indicated that the severity of drought assessments was reasonably accurate compared with the literature. Generally, the current approach is beneficial for describing short-term and/or mild drought episodes. It also accurately evaluated the severe drought events that occurred across a small geographic region. As a result, for small basins and basins with few hydrometeorological stations, it could be the perfect substitute. Future research must concentrate on enhancing the WSDI technique and the classification of severity levels of drought to boost the precision and applicability of this method.

Supplementary Materials: The following supporting information can be downloaded at: <https://www.mdpi.com/article/10.3390/rs15040873/s1>. Figure S1: An example of TWS time series decomposition into seasonal, trend, and remainder components performed using the STL methods; Figure S2: Spatial distribution of Downscaled TWS patterns from 2009.06 to 2010.08 in the IBIS; Figure S3: (a) Comparison between WSDI and inter-annual trend, and (b–f) comparison between STL decomposed inter-annual trends and original data of climatic variables; Figure S4: Comparison of trends between WSDI and climate variables (a) WSDI and precipitation and (b) WSDI and potential evaporation; Figure S5: Comparison of eight drought events identified by total WSD and WSDI during the study. The most severe droughts in 2010 and 2016 are shown with red shading indicate.

Author Contributions: Conceptualization, S.A.; methodology, S.A. and A.T.; validation, S.A.; formal analysis, S.A., B.K., A.T., A.A., I.B., L.Z. and S.S.; investigation, B.K., M.J., M.A., A.A., M.S. and M.A.N.; data curation, S.A., A.T., I.B., A.J. and S.N.K.; writing—original draft preparation, S.A.; writing—review and editing, S.A., B.K., M.J., A.T., M.A., A.A., A.D., I.B., L.Z. and M.S.; visualization, M.J., M.A., M.S., A.D., I.B., L.Z., S.S., M.A.N., A.J. and S.N.K.; supervision, A.T.; Funding, A.T. All authors have read and agreed to the published version of the manuscript.

Funding: This research received no external funding.

Data Availability Statement: Gravity Recovery and Climate Experiment (GRACE) monthly mass grids (RL-06, level-3) processed at the Center for Space Research (CSR, the University of Texas), Jet Propulsion Laboratory (JPL, Pasadena, CA, USA), and GeoForschungsZentrum Potsdam (GFZ, Potsdam, Germany) were downloaded from <https://grace.jpl.nasa.gov/data/get-data/monthly-mass-grids-land/> (accessed on 13 December 2021). Global Land Data Assimilation System (GLDAS) Noah model products were downloaded from <https://disc.gsfc.nasa.gov/datasets> (accessed on 23 November 2021). The monthly TRMM 3B43 product Version 7 was downloaded from <http://disc.sci.gsfc.nasa.gov/precipitation/> (accessed on 5 January 2022). The Digital Elevation Model (DEM) was derived from the Shuttle Radar Topographic Mission (SRTM).

Acknowledgments: The authors would like to thank GRACE Tellus for providing the GRACE Tellus land grid data supported by the NASA Measures Program. The GLDAS data used in this study are acquired as part of the mission of NASA's Earth Science Division and archived and distributed by the Goddard Earth Sciences (GES) Data and Information Services Center (DISC).

Conflicts of Interest: The authors declare no conflict of interest.

References

1. Kogan, F.N. Global Drought Watch from Space. *Bull. Am. Meteorol. Soc.* **1997**, *78*, 621–636. [[CrossRef](#)]
2. Ma, S.; Wu, Q.; Wang, J.; Zhang, S. Temporal evolution of regional drought detected from GRACE TWSA and CCI SM in Yunnan Province. *China. Remote Sens.* **2017**, *9*, 1124. [[CrossRef](#)]
3. Chou, J.; Xian, T.; Dong, W.; Xu, Y. Regional Temporal and Spatial Trends in Drought and Flood Disasters in China and Assessment of Economic Losses in Recent Years. *Sustainability* **2018**, *11*, 55. [[CrossRef](#)]
4. Tariq, A.; Yan, J.; Gagnon, A.; Khan, M.R.; Mumtaz, F. Mapping of cropland, cropping patterns and crop types by combining optical remote sensing images with decision tree classifier and random forest. *Geo-Spatial Inf. Sci.* **2022**, *1*, 1–19. [[CrossRef](#)]
5. Saleem, F.; Arshad, A.; Mirchi, A.; Khaliq, T.; Zeng, X.; Rahman, M.M.; Dilawar, A.; Pham, Q.B.; Mahmood, K. Observed changes in crop yield associated with droughts propagation via natural and human-disturbed agro-ecological zones of Pakistan. *Remote Sens.* **2022**, *14*, 2152. [[CrossRef](#)]
6. Abolafia-Rosenzweig, R.; Pan, M.; Zeng, J.L.; Livneh, B. Remotely sensed ensembles of the terrestrial water budget over major global river basins: An assessment of three closure techniques. *Remote Sens. Env.* **2021**, *252*, 112191. [[CrossRef](#)]

7. Abhishek; Kinouchi, T. Synergetic application of GRACE gravity data, global hydrological model, and in-situ observations to quantify water storage dynamics over Peninsular India during 2002–2017. *J. Hydrol.* **2021**, *596*, 126069. [[CrossRef](#)]
8. Li, J.; Zhang, Q.; Chen, Y.D.; Singh, V.P. GCMs-based spatiotemporal evolution of climate extremes during the 21st century in China. *J. Geophys. Res. Atmos.* **2013**, *118*, 11017–11035. [[CrossRef](#)]
9. Tariq, A.; Jiango, Y.; Li, Q.; Gao, J.; Lu, L.; Soufan, W.; Almutairi, K.F.; Habib-ur-Rahman, M. Modelling, mapping and monitoring of forest cover changes, using support vector machine, kernel logistic regression and naive bayes tree models with optical remote sensing data. *Heliyon* **2023**, *9*, e13212. [[CrossRef](#)]
10. Gu, X.; Li, J.; Chen, Y.D.; Kong, D.; Liu, J. Consistency and Discrepancy of Global Surface Soil Moisture Changes From Multiple Model-Based Data Sets Against Satellite Observations. *J. Geophys. Res. Atmos.* **2019**, *124*, 1474–1495. [[CrossRef](#)]
11. Hina, S.; Saleem, F.; Arshad, A.; Hina, A.; Ullah, I. Droughts over Pakistan: Possible cycles, precursors and associated mechanisms. *Geomat. Nat. Hazards Risk* **2021**, *12*, 1638–1668. [[CrossRef](#)]
12. Ren, Y.; Liu, J.; Shalamzari, M.J.; Arshad, A.; Liu, S.; Liu, T.; Tao, H. Monitoring Recent Changes in Drought and Wetness in the Source Region of the Yellow River Basin, China. *Water* **2022**, *14*, 861. [[CrossRef](#)]
13. Arshad, A.; Zhang, Z.; Zhang, W.; Gujree, I. Long-term prospective changes in crop irrigation requirement caused by climate and agriculture land use changes in Rachna Doab, Pakistan. *Water* **2019**, *11*, 1567. [[CrossRef](#)]
14. Meehl, G.A.; Karl, T.; Easterling, D.R.; Changnon, S.; Pielke, R.; Changnon, D.; Evans, J.; Groisman, P.Y.; Knutson, T.R.; Kunkel, K.E.; et al. An introduction to trends in extreme weather and climate events: Observations, socioeconomic impacts, terrestrial ecological impacts, and model projections. *Bull. Am. Meteorol. Soc.* **2000**, *81*, 413–416. [[CrossRef](#)]
15. Dilawar, A.; Chen, B.; Arshad, A.; Guo, L.; Ehsan, M.I.; Hussain, Y.; Kayiranga, A.; Khaliq, T.; Zeng, X.; Rahman, M.M. Towards Understanding Variability in Droughts in Response to Extreme Climate Conditions over the Different Agro-Ecological Zones of Pakistan. *Sustainability* **2021**, *13*, 6910. [[CrossRef](#)]
16. Shah, S.H.I.A.; Jianguo, Y.; Jahangir, Z.; Tariq, A.; Aslam, B. Integrated geophysical technique for groundwater salinity delineation, an approach to agriculture sustainability for Nankana Sahib Area, Pakistan. *Geomat. Nat. Hazards Risk* **2022**, *13*, 1043–1064. [[CrossRef](#)]
17. Sillmann, J.; Kharin, V.V.; Zwiers, F.W.; Zhang, X.; Bronaugh, D. Climate extremes indices in the CMIP5 multimodel ensemble: Part 2. Future climate projections. *J. Geophys. Res. Atmos.* **2013**, *118*, 2473–2493. [[CrossRef](#)]
18. Dilawar, A.; Chen, B.; Guo, L.; Liu, S.; Shafeeque, M.; Arshad, A.; Hussain, Y.; Khaliq, T.; Zeng, X.; Rahman, M.M. Evaluation the WRF Model with Different Land Surface Schemes: Heat Wave Event Simulations and Its Relation to Pacific Variability over Coastal Region, Karachi, Pakistan. *Sustainability* **2021**, *13*, 12608. [[CrossRef](#)]
19. Baloch, M.Y.J.; Zhang, W.; Chai, J.; Li, S.; Alqurashi, M.; Rehman, G.; Tariq, A.; Talpur, S.A.; Iqbal, J.; Munir, M.; et al. Shallow groundwater quality assessment and its suitability analysis for drinking and irrigation purposes. *Water* **2021**, *13*, 1–25. [[CrossRef](#)]
20. Shah, S.H.I.A.; Yan, J.; Ullah, I.; Aslam, B.; Tariq, A.; Zhang, L.; Mumtaz, F. Classification of Aquifer Vulnerability by Using the DRASTIC Index and Geo-Electrical Techniques. *Water* **2021**, *13*, 2144. [[CrossRef](#)]
21. Hazell, P.; Oram, P.; Chaherli, N. *EPTD Discussion Paper No. 8 Environment and Production Technology Division*; International Food Policy Research Institute: Washington, DC, USA, 2006.
22. Adnan, S.; Ullah, K.; Gao, S. Characterization of drought and its assessment over Sindh, Pakistan during 1951–2010. *J. Meteorol. Res.* **2015**, *29*, 837–857. [[CrossRef](#)]
23. Adnan, S.; Ullah, K.; Gao, S.; Khosa, A.H.; Wang, Z. Shifting of agro climatic zones, their drought vulnerability, and precipitation and temperature trends in Pakistan. *Int. J. Climatol.* **2017**, *37*, 529–543. [[CrossRef](#)]
24. Adnan, S.; Ullah, K.; Shuanglin, L.; Gao, S.; Khan, A.H.; Mahmood, R. Comparison of various drought indices to monitor drought status in Pakistan. *Clim. Dyn.* **2018**, *51*, 1885–1899. [[CrossRef](#)]
25. Tariq, A.; Yan, J.; Ghaffar, B.; Qin, S.; Mousa, B.G.; Sharifi, A.; Huq, M.E.; Aslam, M. Flash Flood Susceptibility Assessment and Zonation by Integrating Analytic Hierarchy Process and Frequency Ratio Model with Diverse Spatial Data. *Water* **2022**, *14*, 3069. [[CrossRef](#)]
26. Abbas, F.; Rehman, I.; Adrees, M.; Ibrahim, M. Prevailing trends of climatic extremes across Indus-Delta of Sindh-Pakistan. *Appl. Clim.* **2018**, *131*, 1101–1117. [[CrossRef](#)]
27. Akhtar, I.U.H. Pakistan Needs a New Crop Forecasting System 2014. Available online: <http://www.scidev.net/en/new-technologies/space-technology/opinions/pakistan-needs-a-newcrop-forecasting-system.html> (accessed on 13 April 2020).
28. Heim, J.R.R. A review of twentieth-century drought indices used in the United States. *Bull. Am. Meteorol. Soc.* **2002**, *83*, 1149–1165. [[CrossRef](#)]
29. Rodell, M.; Famiglietti, J.S.; Wiese, D.N.; Reager, J.T.; Beaudoin, H.K.; Landerer, F.W.; Lo, M.H. Emerging trends in global freshwater availability. *Nature* **2018**, *557*, 651–659. [[CrossRef](#)]
30. Khorrami, B.; Gündüz, O. Detection and analysis of drought over Turkey with remote sensing and model-based drought indices. *Geocarto. Int.* **2022**, *3*, 1–22. [[CrossRef](#)]
31. Van Lanen, H.A.J.; Peters, E. Definition, effects and assessment of groundwater droughts. In *Drought and Drought Mitigation in Europe*; Advances in Natural and Technological Hazards Research; Springer: Berlin/Heidelberg, Germany, 2000; pp. 49–61.
32. Keyantash, J.; Dracup, J.A. The quantification of drought: An evaluation of drought indices. *Bull. Am. Meteorol. Soc.* **2002**, *83*, 1167–1180. [[CrossRef](#)]

33. Wahla, S.S.; Kazmi, J.H.; Sharifi, A.; Shirazi, S.A.; Tariq, A.; Joyell Smith, H. Assessing spatio-temporal mapping and monitoring of climatic variability using SPEI and RF machine learning models. *Geocarto. Int.* **2022**, *1*, 1–20. [[CrossRef](#)]
34. Chen, J.L.; Wilson, C.R.; Tapley, B.D.; Yang, Z.L.; Niu, G. Y 2005 drought event in the Amazon River basin as measured by GRACE and estimated by climate models. *J. Geophys. Res.* **2009**, *114*, B05404. [[CrossRef](#)]
35. Taylor, R.G.; Koussis, A.D.; Tindimuguya, C. Groundwater and climate in Africa—A review. *Hydrol. Sci. J.* **2009**, *54*, 655–664. [[CrossRef](#)]
36. Shahid, S.; Hazarika, M.K. Groundwater drought in the northwestern districts of Bangladesh. *Water Resour. Manag.* **2010**, *24*, 1989–2006. [[CrossRef](#)]
37. Jin, Q.; Wei, J.; Yang, Z.; Wei, J.; Yang, Z. Positive response of Indian summer rainfall to Middle East dust. *Geophys. Res. Lett.* **2014**, *40*, 4068–4074. [[CrossRef](#)]
38. Henderson, J.; Kauffman, N. Initial impacts of the 2012 drought. In *Main Street Economist*; Federal Reserve Bank of Kansas City: Kansas City, MO, USA, 2012; Volume 3, pp. 1–8.
39. Watts, N.; Adger, W.N.; Agnolucci, P.; Othman, A.; Abdelrady, A. Health and climate change: Policy responses to protect public health. *Lancet* **2015**, *386*, 1861–1914. [[CrossRef](#)]
40. Zhai, J.; Huang, J.; Su, B.; Cao, L.; Wang, Y.; Jiang, T.; Fischer, T. Intensity–area–duration analysis of droughts in China 1960–2013. *Clim. Dyn.* **2017**, *48*, 151–168. [[CrossRef](#)]
41. Ahmad, S.; Hussain, Z.; Qureshi, A. *Drought Mitigation in Pakistan: Current Status and Options for Future Strategies*; Working Paper 85; International Water Management Institute: Colombo, Sri Lanka, 2004.
42. Aadhar, S.; Mishra, V. High-resolution near real-time drought monitoring in South Asia. *Sci. Data* **2017**, *4*, 170145. [[CrossRef](#)]
43. Tariq, A.; Mumtaz, F.; Majeed, M.; Zeng, X. Spatio-temporal assessment of land use land cover based on trajectories and cellular automata Markov modelling and its impact on land surface temperature of Lahore district Pakistan. *Environ. Monit. Assess.* **2023**, *195*, 114. [[CrossRef](#)]
44. Jalayer, S.; Sharifi, A.; Abbasi-Moghadam, D.; Tariq, A.; Qin, S. Assessment of Spatiotemporal Characteristic of Droughts Using In Situ and Remote Sensing-Based Drought Indices. *IEEE J. Sel. Top. Appl. Earth Obs. Remote Sens.* **2023**, *16*, 1483–1502. [[CrossRef](#)]
45. Dharpure, J.K.; Goswami, A.; Patel, A.; Longuevergne, L.; Scanlon, B.R. Drought characterization using the Combined Terrestrial Evapotranspiration Index over the Indus, Ganga and Brahmaputra river basins. *Geocarto. Int.* **2020**, *1*, 1–25. [[CrossRef](#)]
46. Thomas, A.C.; Reager, J.T.; Famiglietti, J.S.; Rodell, M. A GRACE-based water storage deficit approach for hydrological drought characterization. *Geophys. Res. Lett.* **2014**, *41*, 1537–1545. [[CrossRef](#)]
47. Jehanzaib, M.; Sattar, M.N.; Lee, J.H.; Kim, T.W. Investigating effect of climate change on drought propagation from meteorological to hydrological drought using multi-model ensemble projections. *Stochastic Environ. Res. Risk Assess* **2020**, *34*, 7–21. [[CrossRef](#)]
48. Mohamed, A.; Faye, C.; Othman, A.; Abdelrady, A. Hydro-Geophysical Evaluation of the Regional Variability of Senegal’s Terrestrial Water Storage Using Time-Variable Gravity Data. *Remote Sens.* **2022**, *14*, 4059. [[CrossRef](#)]
49. Alshehri, F.; Mohamed, A. Analysis of Groundwater Storage Fluctuations Using GRACE and Remote Sensing Data in Wadi As-Sirhan, Northern Saudi Arabia. *Water* **2023**, *15*, 282. [[CrossRef](#)]
50. Abhishek; Kinouchi, T.; Sayama, T. A comprehensive assessment of water storage dynamics and hydroclimatic extremes in the Chao Phraya River Basin during 2002–2020. *J. Hydrol.* **2021**, *603*, 126868. [[CrossRef](#)]
51. Wu, H.; Hayes, M.J.; Wilhite, D.A.; Svoboda, M.D. The effect of the length of record on the standardized precipitation index calculation. *Int. J. Clim.* **2005**, *25*, 505–520. [[CrossRef](#)]
52. Long, D.; Shen, Y.J.; Sun, A.; Hong, Y.; Longuevergne, L.; Yang, Y.T.; Li, B.; Chen, L. Drought and flood monitoring for a large karst plateau in Southwest China using extended GRACE data. *Remote Sens. Env.* **2014**, *155*, 145–160. [[CrossRef](#)]
53. Vicente-Serrano, S.M.; Beguería, S.; López-Moreno, J.I. A Multiscalar Drought Index Sensitive to Global Warming: The Standardized Precipitation Evapotranspiration Index. *J. Clim.* **2010**, *23*, 1696–1718. [[CrossRef](#)]
54. Palmer, W.C. *Meteorological Droughts*; 30 US Department of Commerce; Weather Bureau: Washington, DC, USA, 1965.
55. Wells, N.; Goddard, S.; Hayes, M.J. A self-calibrating palmer drought severity index. *J. Clim.* **2004**, *17*, 2335–2351. [[CrossRef](#)]
56. Hao, Z.; Aghakouchak, A.A. Nonparametric multivariate multi-index drought monitoring framework. *J. Hydrometeorol.* **2014**, *15*, 89–101. [[CrossRef](#)]
57. Liu, B.; Zhou, X.; Li, W. Spatiotemporal characteristics of groundwater drought and its response to meteorological drought in Jiangsu Province, China. *Water* **2016**, *8*, 480. [[CrossRef](#)]
58. Huang, S.; Wang, L.; Wang, H. Spatio-temporal characteristics of drought structure across China using an integrated drought index. *Agric. Water Manag.* **2019**, *218*, 182–192. [[CrossRef](#)]
59. Oliver, J.E. Intergovernmental panel in climate change (IPCC). Encyclopedia Energy Natural Resour. *Environ. Econ.* **2013**, *26*, 48–56.
60. Zhang, X.; Chen, N.; Li, J.; Chen, Z.; Niyogi, D. Multi-sensor integrated framework and index for agricultural drought monitoring. *Remote Sens. Environ.* **2017**, *188*, 141–163. [[CrossRef](#)]
61. Qi, S.; Li, G.; Wang, C. Study on monitoring drought in China with MODIS product. *Adv. Water Sci.* **2005**, *16*, 56–61.
62. Gu, Y.; Brown, J.F.; Verdin, J.P.; Wardlow, B. A five-year analysis of MODIS NDVI and NDWI for grassland drought assessment over the central great plains of the United States. *Geophys. Res. Lett.* **2007**, *34*, 34. [[CrossRef](#)]
63. Long, D.; Scanlon, B.R.; Longuevergne, L.; Sun, A.Y.; Fernando, D.N.; Save, H. GRACE satellite monitoring of large depletion in water storage in response to the 2011 drought in Texas. *Geophys. Res. Lett.* **2013**, *40*, 3395–3401. [[CrossRef](#)]

64. Yi, H.; Wen, L. Satellite gravity measurement monitoring terrestrial water storage change and drought in the continental United States. *Sci. Rep.* **2016**, *6*, 19909. [[CrossRef](#)]
65. Abhishek; Kinouchi, T. Multidecadal Land Water and Groundwater Drought Evaluation in Peninsular India. *Remote Sens* **2022**, *14*, 1486. [[CrossRef](#)]
66. Niemeyer, S. New drought indices. In *Drought Management: Scientific and Technological Innovations, Proceedings of the International Conference Drought Management: Scientific and Technological Innovations, Zaragoza, Spain, 12–14 June 2008*; Options Méditerranéennes: Série A—Séminaires Méditerranéens; López-Francos, A., Ed.; CIHEAM: Zaragoza, Spain, 2008; Volume 1, pp. 267–274, no. 80. Available online: <http://om.ciheam.org/om/pdf/a80/00800451.pdf> (accessed on 12 August 2020).
67. Watkins, M.M.; Wiese, D.N.; Yuan, D.N.; Boening, C.; Landerer, F.W. Improved methods for observing Earth’s time variable mass distribution with GRACE using spherical cap mascons. *J. Geophys. Res. Solid Earth* **2015**, *120*, 2648–2671. [[CrossRef](#)]
68. Wiese, D.N.; Landerer, F.W.; Watkins, M.M. Quantifying and reducing leakage errors in the JPL RL05M GRACE mascon solution. *Water Resour. Res.* **2016**, *52*, 7490–7502. [[CrossRef](#)]
69. Landerer, F.W.; Swenson, S.C. Accuracy of scaled GRACE terrestrial water storage estimates. *Water Resour. Res.* **2012**, *48*, W04531. [[CrossRef](#)]
70. Wahr, J.; Molenaar, M.; Bryan, F. Time variability of the Earth’s gravity field: Hydrological and oceanic effects and their possible detection using GRACE. *J. Geophys. Res. Solid Earth* **1998**, *103*, 30205–30229. [[CrossRef](#)]
71. Ali, S.; Wang, Q.; Liu, D.; Fu, Q.; Rahaman, M.M.; Faiz, M.A.; Cheema, M.J.M. Estimation of spatio-temporal groundwater storage variations in the Lower Transboundary Indus Basin using GRACE satellite. *J. Hydrol.* **2022**, *605*, 123. [[CrossRef](#)]
72. Iqbal, N.; Hossain, F.; Lee, H.; Akhter, G. Integrated groundwater resource management in Indus Basin using satellite gravimetry and physical modeling tools. *Environ. Monit. Assess.* **2017**, *189*, 128. [[CrossRef](#)]
73. Tang, Y.; Hooshyar, M.; Zhu, T.; Ringler, C.; Sun, A.Y.; Long, D.; Wang, D. Reconstructing annual groundwater storage changes in a large-scale irrigation region using GRACE data and Budyko model. *J. Hydrol.* **2017**, *551*, 397–406. [[CrossRef](#)]
74. Hussain, D.; Kao, H.C.; Khan, A.A.; Lan, W.H.; Imani, M.; Lee, C.M.; Kuo, C.Y. Spatial and temporal variations of terrestrial water storage in upper Indus basin using GRACE and altimetry data. *IEEE Access* **2020**, *8*, 65327–65339. [[CrossRef](#)]
75. Akhtar, F.; Nawaz, R.A.; Hafeez, M.; Awan, U.K.; Borgemeister, C.; Tischbein, B. Evaluation of GRACE derived groundwater storage changes in different agro-ecological zones of the Indus Basin. *J. Hydrol.* **2022**, *605*, 127369. [[CrossRef](#)]
76. Arshad, A.; Mirchi, A.; Samimi, M.; Ahmad, B. Combining downscaled-GRACE data with SWAT to improve the estimation of groundwater storage and depletion variations in the Irrigated Indus Basin (IIB). *Sci. Total Env.* **2022**, *838*, 156044. [[CrossRef](#)]
77. Gemtzi, A.; Koutsias, N.; Lakshmi, V. A spatial downscaling methodology for GRACE Total water storage anomalies using GPM IMERG precipitation estimates. *Remote Sens.* **2021**, *13*, 5149. [[CrossRef](#)]
78. Ali, S.; Liu, D.; Fu, Q.; Cheema, M.J.M.; Pham, Q.B.; Rahaman, M.; Dang, T.D.; Anh, D.T. Improving the resolution of GRACE data for spatio-temporal groundwater storage assessment. *Remote Sens.* **2021**, *13*, 3513. [[CrossRef](#)]
79. Vishwakarma, B.D.; Zhang, J.; Sneeuw, N. Downscaling GRACE total water storage change using partial least squares regression. *Sci. Data* **2021**, *8*, 1–13. [[CrossRef](#)]
80. Milewski, A.M.; Thomas, M.B.; Seyoum, W.M.; Rasmussen, T.C. Spatial downscaling of GRACE TWSA data to identify spatiotemporal groundwater level trends in the Upper Floridan Aquifer, Georgia, USA. *Remote Sens.* **2019**, *11*, 2756. [[CrossRef](#)]
81. Seyoum, W.M.; Kwon, D.; Milewski, A.M. Downscaling GRACE TWSA data into high-resolution groundwater level anomaly using machine learning-based models in a glacial aquifer system. *Remote Sens.* **2019**, *11*, 824. [[CrossRef](#)]
82. Chen, L.; He, Q.; Liu, K.; Li, J.; Jing, C. Downscaling of GRACE-Derived Groundwater Storage Based on the Random Forest Model. *Remote Sens.* **2019**, *11*, 2979. [[CrossRef](#)]
83. Yin, W.; Hu, L.; Zhang, M.; Wang, J.; Han, S.C. Statistical Downscaling of GRACE-Derived Groundwater Storage Using ET Data in the North China Plain. *J. Geophys. Res. Atmos.* **2018**, *123*, 5973–5987. [[CrossRef](#)]
84. Rahaman, M.M.; Thakur, B.; Kalra, A.; Li, R.; Maheshwari, P. Estimating High-Resolution Groundwater Storage from GRACE: A Random Forest Approach. *Environments* **2019**, *6*, 63. [[CrossRef](#)]
85. Ning, S.; Ishidaira, H.; Wang, J. Statistical downscaling of GRACE-derived terrestrial water storage using satellite and gldas products. *J. Jpn. Soc. Civ. Eng.* **2014**, *70*, I_133–I_138. [[CrossRef](#)]
86. Zhu, Y.; Liu, S.; Yi, Y.; Xie, F.; Grünwald, R.; Miao, W.; Wu, K. Science of the Total Environment. Overview of terrestrial water storage changes over the Indus River Basin based on GRACE/GRACE-FO solutions. *Sci. Total Environ.* **2021**, *799*, 149366. [[CrossRef](#)]
87. Ali, S.; Liu, D.; Fu, Q.; Cheema, M.J.M.; Pal, S.C.; Arshad, A.; Pham, Q.B.; Zhang, L. Constructing high-resolution groundwater drought at spatio-temporal scale using GRACE satellite data based on machine learning in the Indus Basin. *J. Hydrol.* **2022**, *12*, 8295, ISSN 0022-1694. [[CrossRef](#)]
88. Shamsudduha, M.; Panda, D.K. International Journal of Disaster Risk Reduction Spatio-temporal changes in terrestrial water storage in the Himalayan river basins and risks to water security in the region: A review. *Int. J. Disaster Risk Reduct.* **2019**, *35*, 101068. [[CrossRef](#)]
89. Siebert, S.; Kumm, M.; Porkka, M.; Döll, P.; Ramankutty, N.; Scanlon, B. A global data set of the extent of irrigated land from 1900 to 2005. *Hydrol. Earth Syst. Sci.* **2015**, *19*, 1521–1545. [[CrossRef](#)]
90. Ullah, M.K.; Habib, Z.; Muhammad, S. *Spatial Distribution of Reference and Potential Evapotranspiration across the Indus Basin Irrigation Systems*; IWMI Working Paper; IWMI: Lahore, Pakistan, 2001; Volume 24.

91. Khorrami, B.; Gunduz, O. An enhanced water storage deficit index (EWSDI) for drought detection using GRACE gravity estimates. *J. Hydrol.* **2021**, *603*, 126812. [[CrossRef](#)]
92. Huffman, G.J.; Adler, R.F.; Bolvin, D.T.; Gu, G.J.; Nelkin, E.J.; Bowman, K.P.; Hong, Y.; Stocker, E.F.; Wolff, D.B. The TRMM multisatellite precipitation analysis (TMPA): Quasi-global, multiyear, combined-sensor precipitation estimates at fine scales. *J. Hydrometeorol.* **2007**, *8*, 38–55. [[CrossRef](#)]
93. Cheema, M.J.M.; Bastiaanssen, W.G.M. Local calibration of remotely sensed rainfall from the TRMM satellite for different periods and spatial scales in the Indus Basin. *Int. J. Remote Sens.* **2012**, *33*, 2603–2627. [[CrossRef](#)]
94. Rodell, M.; Houser, P.; Jambor, U.; Gottschalck, J.; Mitchell, K.; Meng, C.-J.; Arsenault, K.; Cosgrove, B.; Radakovich, J.; Bosilovich, M. The global land data assimilation system. *Bull. Am. Meteorol. Soc.* **2004**, *85*, 381–394. [[CrossRef](#)]
95. Yang, T.; Wang, C.; Yu, Z.; Xu, F. Characterization of spatio-temporal patterns for various GRACE- and GLDAS-born estimates for changes of global terrestrial water storage. *Glob. Planet. Chang.* **2013**, *109*, 30–37. [[CrossRef](#)]
96. Long, D.; Longuevergne, L.; Scanlon, B.R. Uncertainty in evapotranspiration from land surface modeling, remote sensing, and GRACE satellites. *Water Resour. Res.* **2014**, *50*, 1131–1151. [[CrossRef](#)]
97. Sun, Z.; Long, D.; Yang, W.; Li, X.; Pan, Y. Reconstruction of GRACE data on changes in total water storage over the global land surface and 60 basins. *Water Resour. Res.* **2020**, *55*, e2019WR026250. [[CrossRef](#)]
98. Abdi, H.; Lynne, J.W. Partial least squares methods: Partial least squares correlation and partial least square regression. In *Computational toxicology*; Brad, R., Arthur, N.M., Eds.; Humana Press: New York, NY, USA, 2013; pp. 549–579. [[CrossRef](#)]
99. Woldesenbet, T.A.; Elagib, N.A.; Ribbe, L.; Heinrich, J. Hydrological responses to land use/cover changes in the source region of the Upper Blue Nile Basin, Ethiopia. *Sci. Total Environ.* **2017**, *575*, 724–741. [[CrossRef](#)]
100. Yuan, R.Q.; Chang, L.L.; Gupta, H.; Niu, G.Y. Climatic forcing for recent significant terrestrial drying and wetting. *Adv. Water Resour.* **2019**, *133*, 103425. [[CrossRef](#)]
101. Wu, T.; Zheng, W.; Yin, W.; Zhang, H. Spatiotemporal Characteristics of Drought and Driving Factors Based on the GRACE-Derived Total Storage Deficit Index: A Case Study in Southwest China. *Remote Sens.* **2021**, *13*, 79. [[CrossRef](#)]
102. Cleveland, R.B.; Cleveland, W.S.; Terpenning, I. STL: A seasonal-trend decomposition procedure based on loess. *J. Off. Stat.* **1990**, *6*, 3–73.
103. Bergmann, I.; Ramillien, G.; Frappart, F. Climate-driven interannual ice mass evolution in Greenland. *Glob. Planet. Chang.* **2012**, *82–83*, 1–11. [[CrossRef](#)]
104. Frappart, F.; Ramillien, G.; Ronchail, J. Changes in terrestrial water storage versus rainfall and discharges in the Amazon basin. *Int. J. Clim.* **2013**, *33*, 3029–3046. [[CrossRef](#)]
105. Sun, Z.L.; Zhu, X.F.; Pan, Y.Z.; Zhang, J.S.; Liu, X.F. Drought evaluation using the GRACE terrestrial water storage deficit over the Yangtze River Basin, China. *Sci. Total Environ.* **2018**, *634*, 727–738. [[CrossRef](#)]
106. Chen, T.; Guestrin, C. Xgboost: A scalable tree boosting system. In Proceedings of the 22nd ACM SIGKDD International Conference on Knowledge Discovery and Data Mining, San Francisco, CA, USA, 13–17 August 2016; pp. 785–794.
107. Zhu, S.; Zhu, F. Cycling comfort evaluation with instrumented probe bicycle. *Transp. Res. Part A Policy Pr.* **2019**, *129*, 217–231. [[CrossRef](#)]
108. Chen, H.; Chen, H.; Liu, Z.; Sun, X.; Zhou, R. Analysis of Factors Affecting the Severity of Automated Vehicle Crashes Using XGBoost Model Combining POI Data. *J. Adv. Transp.* **2020**, *4*, 1–12. [[CrossRef](#)]
109. Chen, T.; He, T.; Benesty, M.; Khotilovich, V. Package ‘xgboost’. *R version*. 2020, Volume 90. Available online: <https://cran.rproject.org/web/packages/xgboost/index.html> (accessed on 5 January 2020).
110. Zolfaghari, A.; Izadi, M. Burst Pressure Prediction of Cylindrical Vessels Using Artificial Neural Network. *J. Press. Vessel Technol.* **2020**, *142*, 031303. [[CrossRef](#)]
111. Gholami, V.; Booij, M.J.; Nikzad Tehrani, E.; Hadian, M.A. Spatial Soil Erosion Estimation Using an Artificial Neural Network (ANN) and Field Plot Data. *Catena* **2018**, *163*, 210–218. [[CrossRef](#)]
112. Mohaghegi, S.; Del Valle, Y.; Venayagamoorthy, G.K.; Harley, R.G. A Comparison of PSO and Backpropagation for Training RBF Neural Networks for Identification of a Power System with Statcom. In Proceedings of the 2005 IEEE Swarm Intelligence Symposium, Pasadena, CA, USA, 1–3 March 2005; pp. 391–394.
113. Turban, E.; Sharda, R.; Aronson, J.E.; King, D.N. *Business Intelligence: A Managerial Approach*; Pearson Prentice Hall: Upper Saddle River, NJ, USA, 2008.
114. Zhang, Y.; He, B.; Guo, L.; Liu, D. Differences in response of terrestrial water storage components to precipitation over 168 global river basins. *J. Hydrometeorol.* **2019**, *20*, 1981–1999. [[CrossRef](#)]
115. Brydsten, L. *Modelling Groundwater Discharge Areas Using Only Digital Elevation Models as Input Data*; Swedish Nuclear Fuel and Waste Management, Co.: Stockholm, Sweden, 2006.
116. Li, J.; Wong, D.W.S. Effects of DEM sources on hydrologic applications. *Comput. Environ. Urban Syst.* **2010**, *34*, 251–261. [[CrossRef](#)]
117. Mirosław-Swiątek, D.; Kiczko, A.; Szporak-Wasilewska, S.; Grygoruk, M. Too wet and too dry? Uncertainty of DEM as a potential source of significant errors in a model-based water level assessment in riparian and mire ecosystems. *Wetl. Ecol. Manag.* **2017**, *25*, 547–562. [[CrossRef](#)]
118. Li, W.; Wang, W.; Zhang, C.Y.; Yang, Q.; Feng, W.; Liu, Y. Monitoring groundwater storage variations in the Guanzhong area using GRACE satellite gravity data. *Chin. J. Geophys.* **2018**, *6*, 2237–2245.

119. Zhen, L.; Chuanyin, Z.; Baogui, K.; Yang, L.; Wanqiu, L.; Cai, Y. North China Plain water storage variation analysis based on GRACE and seasonal influence considering. *Acta Geod. Cartogr. Sin.* **2018**, *47*, 940–949.
120. Zhong, Y.; Zhong, M.; Feng, W.; Zhang, Z.; Shen, Y.; Wu, D. Groundwater depletion in the West Liaohe River Basin, China and its implications revealed by GRACE and in situ measurements. *Remote Sens.* **2018**, *10*, 493. [[CrossRef](#)]
121. Zhang, S.; Wu, Y.; Sivakumar, B.; Mu, X.; Zhao, F.; Sun, P.; Sun, Y.; Qiu, L.; Chen, J.; Meng, X.; et al. Climate change-induced drought evolution over the past 50 years in the southern Chinese Loess Plateau. *Environ. Model. Softw.* **2019**, *122*, 104519. [[CrossRef](#)]
122. Buma, W.G.; Lee, S.-I. Multispectral image-based estimation of drought patterns and intensity around lake Chad, Africa. *Remote Sens.* **2019**, *11*, 2534. [[CrossRef](#)]
123. Seyoum, W.M.; Milewski, A.M. Improved methods for estimating local terrestrial water dynamics from GRACE in the northern high plains. *Adv. Water Resour. Res.* **2017**, *110*, 279–290. [[CrossRef](#)]
124. Cao, Y.P.; Nan, Z.T.; Cheng, G.D. GRACE gravity satellite observations of terrestrial water storage changes for drought characterization in the arid land of Northwestern China. *Remote Sens.* **2015**, *7*, 1021–1047. [[CrossRef](#)]
125. Sun, A.Y.; Scanlon, B.R.; Save, H.; Rateb, A. Reconstruction of GRACE total water storage through automated machine learning. *Water Resour. Res.* **2021**, *57*, e2020WR028666. [[CrossRef](#)]
126. Long, D.; Yang, Y.; Wada, Y.; Hong, Y.; Liang, W.; Chen, Y.; Yong, B.; Hou, A.; Wei, J.; Chen, L. Deriving scaling factors using a global hydrological model to restore GRACE total water storage changes for China's Yangtze River Basin. *Remote Sens. Env.* **2015**, *168*, 177–193. [[CrossRef](#)]
127. Kumar, K.S.; Rathnam, E.V.; Sridhar, V. Tracking seasonal and monthly drought with GRACE-based terrestrial water storage assessments over major river basins in South India. *Sci. Total Env.* **2020**, *763*, 142994. [[CrossRef](#)] [[PubMed](#)]
128. Becker, M.; Meyssignac, B.; Xavier, L.; Cazenave, A.; Alkama, R.; Decharme, B. Past terrestrial water storage (1980–2008) in the Amazon Basin reconstructed from GRACE and in situ river gauging data. *Hydrol. Earth Syst. Sci.* **2011**, *15*, 533–546. [[CrossRef](#)]
129. Humphrey, V.; Gudmundsson, L.; Seneviratne, S.I. A global reconstruction of climate-driven subdecadal water storage variability. *Geophys. Res. Lett.* **2017**, *44*, 2300–2309. [[CrossRef](#)]
130. Maybank, J.; Bonsai, B.; Jones, K.; Lawford, R.; O'Brien, E.G.; Ripley, E.A.; Wheaton, E. Drought as a natural disaster. *Atmos.-Ocean* **1995**, *33*, 195–222. [[CrossRef](#)]
131. Mo, K.C. Drought onset and recovery over the United States. *J. Geophys. Res.* **2011**, *116*, D20106. [[CrossRef](#)]
132. Miro, M.E.; Famiglietti, J.S. Downscaling GRACE Remote Sensing Datasets to High-Resolution Groundwater Storage Change Maps of California's Central Valley. *Remote Sens.* **2018**, *10*, 143. [[CrossRef](#)]
133. Yirdaw, S.Z.; Snelgrove, K.R.; Agboma, C.O. GRACE satellite observations of terrestrial moisture changes for drought characterization in the Canadian Prairie. *J. Hydrol.* **2008**, *356*, 84–92. [[CrossRef](#)]
134. Tang, Q.H.; Zhang, X.J.; Tang, Y. Anthropogenic impacts on mass change in North China. *Geophys. Res. Lett.* **2013**, *40*, 3924–3928. [[CrossRef](#)]

Disclaimer/Publisher's Note: The statements, opinions and data contained in all publications are solely those of the individual author(s) and contributor(s) and not of MDPI and/or the editor(s). MDPI and/or the editor(s) disclaim responsibility for any injury to people or property resulting from any ideas, methods, instructions or products referred to in the content.